ARTICLES
https://doi.org/10.1038/s41564-022-01206-9
nature microbiology

Check for updates

Bacterial divisome protein FtsA forms curved antiparallel double filaments when binding to FtsN

Tim Nierhaus[1], Stephen H. McLaughlin[1], Frank Bürmann[1], Danguole Kureisaite-Ciziene[1], Sarah L. Maslen[1,2], J. Mark Skehel[1,2], Conny W. H. Yu[1], Stefan M. V. Freund[1], Louise F. H. Funke[1], Jason W. Chin[1] and Jan Löwe[1]✉

During bacterial cell division, filaments of tubulin-like FtsZ form the Z-ring, which is the cytoplasmic scaffold for divisome assembly. In *Escherichia coli*, the actin homologue FtsA anchors the Z-ring to the membrane and recruits divisome components, including bitopic FtsN. FtsN regulates the periplasmic peptidoglycan synthase FtsWI. To characterize how FtsA regulates FtsN, we applied electron microscopy to show that *E. coli* FtsA forms antiparallel double filaments on lipid monolayers when bound to the cytoplasmic tail of FtsN. Using X-ray crystallography, we demonstrate that *Vibrio maritimus* FtsA crystallizes as an equivalent double filament. We identified an FtsA–FtsN interaction site in the IA–IC interdomain cleft of FtsA using X-ray crystallography and confirmed that FtsA forms double filaments in vivo by site-specific cysteine cross-linking. FtsA–FtsN double filaments reconstituted in or on liposomes prefer negative Gaussian curvature, like those of MreB, the actin-like protein of the elongasome. We propose that curved antiparallel FtsA double filaments together with treadmilling FtsZ filaments organize septal peptidoglycan synthesis in the division plane.

The cell shape of non-spherical walled bacteria is determined by a load-bearing structure counteracting turgor pressure named the peptidoglycan sacculus[1]. Insertion of newly synthesized glycan strands into the sacculus is mediated by the divisome in cell division and the elongasome (or rod complex) in cell elongation[2]. In *Escherichia coli*, both of these multiprotein complexes span the entire cell envelope, and contain the cytoplasmic, membrane-binding and filament-forming actin homologues FtsA (divisome) and MreB (elongasome)[3,4].

In *E. coli* and many other bacteria, FtsA is the main membrane anchor for the cell division ring, the Z-ring, which initiates and organizes division[5]. ZipA can function as an alternative membrane anchor for the Z-ring but seems to have a minor role in cell division in unperturbed cells[5]. The Z-ring is mainly formed by filaments of the tubulin homologue FtsZ[6–8]. FtsZ treadmilling dynamics, driven by the GTPase activity of FtsZ, were shown to be essential for the initial condensation of FtsZ filaments into the Z-ring but seem to become dispensable after partial constriction of the septum[9–11].

Apart from localizing FtsZ to the membrane, FtsA is also involved in the recruitment of essential divisome proteins such as FtsK, FtsN and potentially FtsQ[12,13]. Together with the bitopic membrane protein FtsN, FtsA forms an interaction that is crucial for the recruitment of divisome components[14]. Most of FtsN assembles last into the divisome and activates or regulates the bipartite septal peptidoglycan synthase FtsWI via FtsQLB[15–19]. Small amounts of FtsN are recruited early to the divisome in a FtsA-dependent manner[20].

FtsA has a uniquely positioned IC domain among actin homologues[21]. The FtsA IC domain is important for the interaction with the cytoplasmic tail of FtsN, which comprises approximately 32 amino acids in *E. coli*[22–26]. Two FtsN-suppressor mutations in FtsA located in its IC domain[16,27] further support the idea that FtsN binds the IC domain of FtsA. In FtsN, a conserved stretch of basic amino acids in its amino (N)-terminal cytoplasmic tail is required for interaction with FtsA in vitro[22,24]. In a *zipA*-null background, in which the FtsA–FtsN interaction becomes essential, mutation of the basic stretch in FtsN is however permissible, whereas a D5N mutation is not[23]. Together with previous yeast two-hybrid assays[28], it was suggested that interaction with FtsN depolymerizes FtsA and thereby allows recruitment of downstream divisome components via binding sites that were (partially) occluded in the FtsA polymer[14,23]. Through Förster resonance energy transfer microscopy, the hypermorphic FtsA* mutant was found to be less polymeric than wild-type FtsA on supported lipid bilayers[29]. However, the addition of cytoplasmic FtsN peptide in those experiments induced FtsA* polymerization to levels comparable to wild-type FtsA, challenging the previous model that FtsN depolymerizes FtsA.

Despite the uniqueness of the IC domain of FtsA amongst the actin-like proteins[21], FtsA was shown to form single protofilaments that recapitulate some structural features of bona fide actin protofilaments[30]. Double filaments were shown to be the smallest functional unit of all other known actin homologues[31] and *Thermotoga maritima* FtsA was indeed also shown to form double filaments[30]. More recently, several mutations in *E. coli* FtsA, originally described as ZipA-suppressor mutations, were shown to facilitate double-filament formation of FtsA on supported lipid monolayers[32].

Similar to FtsA, *E. coli* MreB—the actin-like protein of the elongasome—binds membranes directly through an amphipathic helix and forms curved antiparallel double filaments[4,33,34]. This enables a curvature-sensing mechanism that allows MreB filaments to align with the axis of highest principal curvature, the short axis of the cell in the case of rod-shaped cells such as *Bacillus subtilis*[34,35]. Hence, the elongasome uses MreB double filaments as 'rudders' to direct movement of its bipartite peptidoglycan synthase RodA–PBP2 (similar to FtsWI in the divisome) and thereby directs insertion of new peptidoglycan strands around the cell circumference[36]. It is thought that the radially inserted peptidoglycan hoops enforce rod shape by mechanically limiting cell-width expansion.

[1]MRC Laboratory of Molecular Biology, Cambridge, UK. [2]Present address: The Francis Crick Institute, London, UK. ✉e-mail: jyl@mrc-lmb.cam.ac.uk

Here we investigated how FtsA functions in the divisome in bacteria using structural and genetic approaches. We characterize the interaction between *E. coli* FtsA and FtsN and its effect on the architecture of FtsA double filaments. We propose a curvature-based mechanism by which FtsA filaments contribute to oriented peptidoglycan synthesis.

Results

***Vibrio maritimus* FtsA crystallizes as an antiparallel double filament.** We solved the crystal structures of carboxy (C)-terminally truncated FtsAs from *E. coli* (EcFtsA; Protein Data Bank (PDB) identifier: 7Q6D) and the closely related Gram-negative bacteria *Xenorhabdus poinarii* (XpFtsA; PDB 7Q6G; 90% identity to EcFtsA) and *V. maritimus* (VmFtsA; PDB 7Q6F; 70% identity to EcFtsA) (Supplementary Table 1). The EcFtsA$^{1-405}$ and XpFtsA$^{1-396}$ structures showed single protofilaments with a 'loose' longitudinal contact between the IIA and IIB subdomains (Extended Data Fig. 1a). In contrast, VmFtsA$^{1-396}$ crystallized as straight antiparallel double filaments, with lateral contacts formed by the IC domain, which among actins is unique to FtsA[21] (Fig. 1a). The longitudinal interface contact between the IIA and IIB domains was 'tight' in both protofilaments, as was the case previously for TmFtsA bound to ATP-γ-S (PDB 4A2B, ref. [30]; Extended Data Fig. 1a). We noticed that the position of the IC domain is variable within FtsA monomers across FtsA structures (Extended Data Fig. 1b). The positioning of the IC domain does not correlate with species or the presence of continuous protofilaments in the crystal, as analysed for PDB 1E4F, 4A2B and 7Q6F.

The lateral interface in the VmFtsA double filament is almost exclusively formed by contacts between IC domains (Fig. 1b). Each FtsA monomer contacts two subunits in the opposing protofilament, forming the FtsA$_i$–FtsA$_{i*}$ and FtsA$_i$–FtsA$_{i*-1}$ lateral interfaces. Both interfaces have local twofold (C2) symmetry, as indicated in Fig. 1b. The VmFtsA double filament is wider than the MreB double filament (PDB 4CZJ)[33], which is, like FtsA filaments, comprised of two antiparallel protofilaments (Extended Data Fig. 1c). The membrane-proximal side of the FtsA and MreB double filaments is flat. ZipA-suppressor mutations in *E. coli* FtsA (including FtsA^{R286W}, also known as FtsA*), which were described to also affect filament architecture[32] (Supplementary Table 2), correspond to residues in subunit interfaces in the VmFtsA double-filament structure (Fig. 1c). Interestingly, the FtsN-suppressor mutations E124A[27] and I143L[16] described for *E. coli* FtsA also map to subunit interfaces in the VmFtsA double-filament structure (Fig. 1c).

***E. coli* FtsA forms antiparallel double filaments with EcFtsN$^{1-32}$.** As described previously[37], we found that *E. coli* FtsA forms 'mini-rings' on supported lipid monolayers (Fig. 2a, wild type + no peptide). Given that filament-architecture mutations and FtsN-suppressor mutations in *E. coli* FtsA map to lateral interfaces in the VmFtsA double filament (Fig. 1c), we hypothesized that FtsN could affect the formation of *E. coli* FtsA double filaments. The short cytoplasmic tail of FtsN (comprising approximately 32 amino acids in *E. coli*; Extended Data Fig. 2a) interacted with FtsA, as shown previously[20,22,23]. Using surface plasmon resonance (SPR), we demonstrated that EcFtsN$^{1-32}$ binds EcFtsA and EcFtsA$^{1-405}$ (a C-terminal truncation of EcFtsA lacking the amphipathic membrane-binding helix) with dissociation constants (K_d) of 0.8 μM and 2.0 μM, respectively (Fig. 2b). The interaction between *V. maritimus* FtsA$^{1-396}$ and FtsN$^{1-29}$ was about threefold weaker than the EcFtsA$^{1-405}$–EcFtsN$^{1-32}$ interaction (Extended Data Fig. 2b). Given that cross-linking of FtsA to the flow cell surface in SPR might affect FtsA polymerization, we also probed the FtsA–FtsN interaction in solution using fluorescence polarization, for which C-terminally truncated FtsA was titrated into Atto 495-labelled FtsN peptide. The fluorescence polarization data were fitted to a two-step model with K_d values of about 0.016 μM and 11 μM for the EcFtsA$^{1-405}$–FtsN$^{1-32}$-C–Atto 495 interaction (Fig. 2c). The VmFtsA$^{1-396}$–FtsN$^{1-29}$-C–Atto 495 interaction was about fourfold weaker for the first binding event (Extended Data Fig. 2c). Next, we subjected the system to analytical ultracentrifugation using a fluorescence detection system (FDS–AUC) to characterize the two binding events of the FtsA–FtsN interaction. The FDS–AUC experiments showed that both binding events are accompanied by the formation of higher-order FtsA–FtsN assemblies, indicating that the cytoplasmic FtsN peptide not only binds to FtsA but could also facilitate FtsA polymerization (Fig. 2d and Extended Data Fig. 2d). Using a co-pelleting assay, for which cytoplasmic FtsN peptide was titrated into truncated FtsA, we observed that FtsN peptide indeed induces FtsA polymerization (Fig. 2e and Extended Data Fig. 2e).

Given that the cytoplasmic peptide of FtsN induces FtsA polymerization, we next investigated the architecture of those polymers using negative-stain electron microscopy. Both EcFtsA–FtsN$^{1-32}$ and VmFtsA–FtsN$^{1-29}$ formed short double filaments on supported lipid monolayers (Fig. 2a, wild type and Extended Data Fig. 2f). Cryogenic electron microscopy (cryo-EM) imaging and subsequent two-dimensional (2D) averaging of EcFtsA–FtsN$^{1-32}$ double filaments on lipid monolayers showed that EcFtsA–FtsN$^{1-32}$ double filaments have an architecture very similar to the VmFtsA$^{1-396}$ double filaments, determined by crystallography (PDB 7Q6F; Fig. 2f). To corroborate, we designed a lateral interface mutant of *E. coli* FtsA based on the VmFtsA double-filament structure EcFtsA^{M96E,R153D} (Fig. 2g, right). The lipid monolayer assay showed that EcFtsA^{M96E,R153D} was indeed deficient in EcFtsN$^{1-32}$-dependent double-filament formation (Fig. 2g).

The short cytoplasmic tail of FtsN harbours two sequence motifs that are conserved among *E. coli* and related proteobacteria with similar FtsA and FtsN sequences: a conserved ^{3}R/KDY^{6} (*E. coli* amino-acid positions) motif near the N terminus[23] and two to three stretches of basic amino acids, with the most prominent in *E. coli* FtsN being ^{16}RRKK^{19} (ref. [22]) (Extended Data Fig. 2a,g). In *E. coli*, a D5N mutation in the conserved N-terminal motif of FtsN was shown to impair FtsA–FtsN interactions in vivo[23] but did not affect binding or co-localization with FtsA–FtsZ filaments on supported lipid bilayers in vitro[24]. In contrast, and somewhat confusingly, mutation of the basic ^{16}RRKK^{19} stretch abrogated binding in vitro[22,24] yet was permissible in vivo under conditions for which the FtsA–FtsN interaction becomes essential[23]. We therefore tested a set of EcFtsN$^{1-32}$ truncations and mutations in our SPR and monolayer assays to determine the effect of those modifications on the FtsA–FtsN interaction and on double-filament formation (Extended Data Fig. 2h,i). Mutation or deletion of any one of the three stretches of basic amino acids in EcFtsN$^{1-32}$ reduced the binding affinity for FtsA and consequently its ability to promote the formation of FtsA double filaments. EcFtsN$^{1-32,\ D5N}$ and EcFtsN$^{1-33,\ scrambled}$ (Supplementary Table 5) did not show reduced binding affinity but were unable to induce the formation of FtsA double filaments. Hence, the D5N mutation in FtsN might be non-permissible in vivo under conditions for which the FtsA–FtsN interaction becomes essential because it fails to promote the formation of FtsA double filaments. In other words, this result supports the idea that FtsA double filaments are important for the activation or correct regulation of cell division by FtsA and FtsN.

We then tested whether any of the FtsN-suppressor[16,27] or filament-architecture and ZipA-suppressor mutations[32] in FtsA (mutants summarized in Supplementary Table 2) would impact FtsN-induced double-filament formation of FtsA (Fig. 1c). Although the FtsN-suppressor mutants FtsA^{E124A} and FtsA^{I143L}, similar to wild-type FtsA, formed mini-rings in the absence of EcFtsN$^{1-32}$, they more readily formed double filaments than wild-type FtsA at a three- (7 μM) and sixfold (13 μM) molar excess of EcFtsN$^{1-32}$ (Fig. 2a). The filament-architecture and ZipA-suppressor mutants

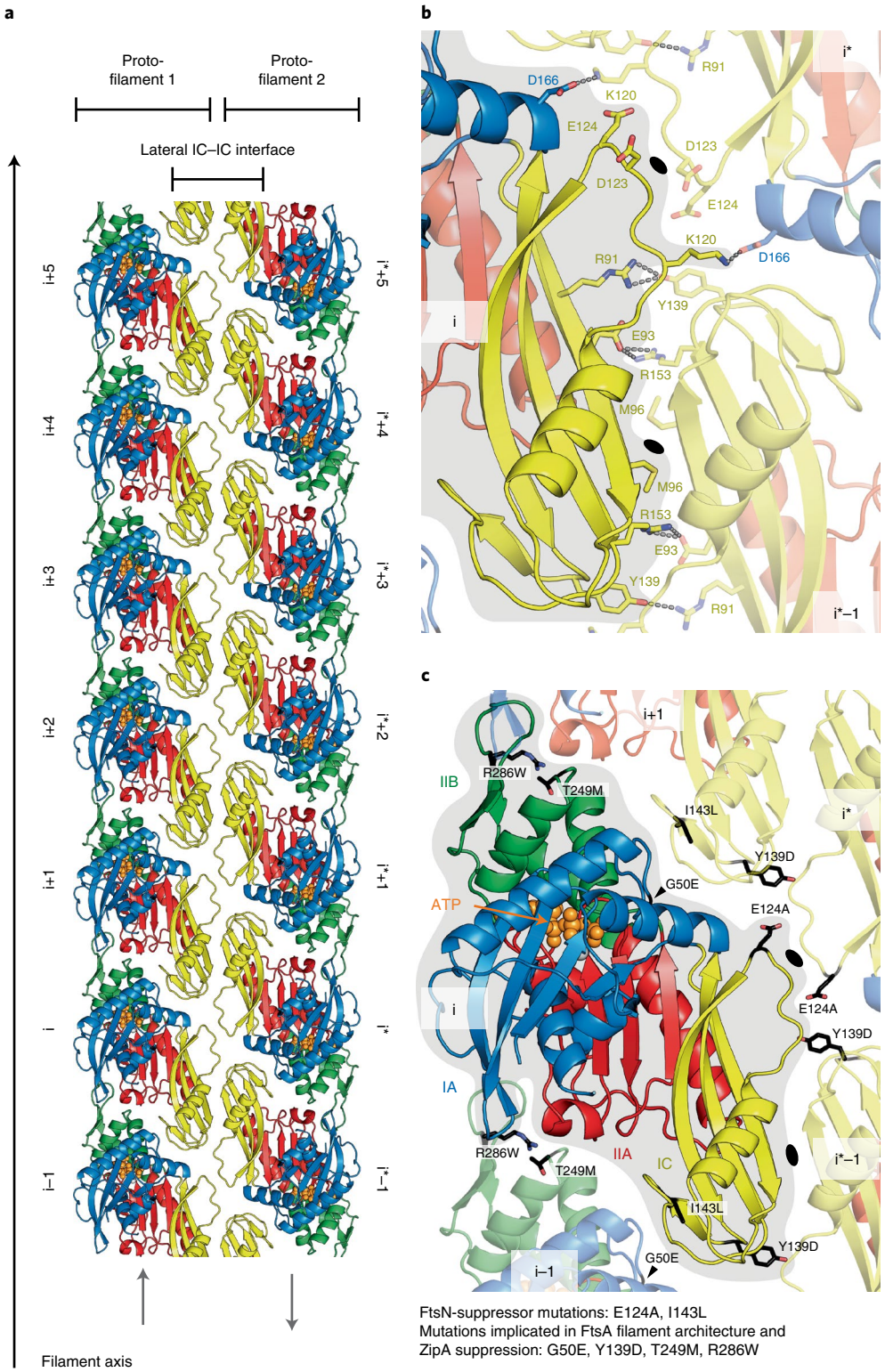

Fig. 1 | VmFtsA crystallizes as an antiparallel double filament via IC domains. a, Top view of the VmFtsA$^{1-396}$ antiparallel double filament in a cartoon representation from the membrane-proximal side (PDB 7Q6F). The lateral interface is almost exclusively formed by the IC domain (yellow). The grey arrows indicate the relative orientations of FtsA monomers in each protofilament. **b**, Side-chain interactions in the lateral filament interface. Each FtsA$_i$ contacts two neighbouring FtsAs, FtsA$_{i^*-1}$ and FtsA$_{i^*}$ in the opposing protofilament. Both interfaces have local C2 symmetry (black ellipses). **c**, Reported FtsN-suppressor mutations in *E. coli* FtsA, E124A[27] and I143L[16], and ZipA-suppressor mutations that have been recently implicated in FtsA (double) filament formation[32] are mapped on the VmFtsA double-filament structure. All mutations are part of filament interfaces. For further information about the suppressor mutants, see Supplementary Table 2.

FtsA^{G50E} and FtsA^{R286W} formed fewer mini-rings than wild-type FtsA in the absence of FtsN (Fig. 2a). Mini-rings and short double filaments were observed for FtsA^{G50E}. FtsA^{R286W} predominantly formed arcs, curved, short and single filaments. Similar to the FtsA^{E124A} and FtsA^{I143L} proteins, FtsA^{G50E} and FtsA^{R286W} formed many more double filaments than wild-type FtsA at a three- (7 μM) and sixfold (13 μM) molar excess of EcFtsN$^{1–32}$ (Fig. 2a). Thus, both FtsN-suppressor as well as ZipA-suppressor and FtsA filament-architecture mutants seem to enhance the formation of FtsN-dependent FtsA double filaments.

VmFtsN$^{1–29}$ binds VmFtsA$^{1–396}$ in the IA–IC interdomain cleft. To understand the FtsA–FtsN interaction at the molecular level, we co-crystallized VmFtsA$^{1–396}$ with the *V. maritimus* cytoplasmic FtsN peptide VmFtsN$^{1–29}$. The VmFtsA$^{1–396}$–VmFtsN$^{1–29}$ co-crystal structure (PDB 7Q6I) showed a larger unit cell than that obtained for the VmFtsA$^{1–396}$ double-filament structure (PDB 7Q6F; two FtsA monomers per asymmetric unit), encompassing 16 FtsA monomers per asymmetric unit (Supplementary Table 1). The 16 FtsA monomers are organized into four tetramers, each containing two short antiparallel protofilaments comprising two FtsA monomers (Fig. 3a and Supplementary Video 1). One of the two FtsA monomers in each protofilament adopts a closed conformation and the other an open conformation (Extended Data Fig. 3a). The positions of the IC domains in the closed (PDB 7Q6I, chain A) and open (PDB 7Q6I, chain B) conformation are similar but not identical to the IC domain position in the VmFtsA$^{1–396}$ double filament (PDB 7Q6F; Extended Data Fig. 1b). Only in the IA–IC interdomain cleft of closed FtsA monomers could we observe electron density for the VmFtsN$^{1–29}$ peptide (Fig. 3a,d and Extended Data Fig. 3a). The IC domain in the open conformation is rotated downwards by 13.8° compared with the closed conformation, as analysed by DynDom[38] (Extended Data Fig. 3a). This means that the open conformation is probably incompatible with VmFtsN$^{1–29}$ binding (Extended Data Fig. 3a). The IC domains in the lateral interfaces of each tetramer are twisted against each other compared with the straight VmFtsA$^{1–396}$ double filament (Fig. 3a). Several hydrogen bonding contacts are lost because of the bending when compared with the straight filament (Fig. 3a, asterisks and Fig. 3b). The VmFtsA$^{1–396}$–VmFtsN$^{1–29}$ tetramer is bent along the filament axis with an estimated radius of curvature of 16.3 nm (Fig. 3b). We noticed that symmetry expansion of a longitudinal dimer present in the VmFtsA$^{1–396}$–VmFtsN$^{1–29}$ tetramer results in a helix with a diameter of approximately 20 nm, matching the diameter reported for FtsA mini-rings[37]. A comparison between the atomic model of the symmetry-expanded helix and a cryo-EM 2D class average of EcFtsA mini-rings assembled on lipid monolayers showed that the IA domain of FtsA faces outwards in the mini-rings (Extended Data Fig. 3b). In contrast to a previous study[37], approximately 65% of the intact mini-rings we observed were comprised of 13 FtsA monomers, whereas 35% were 12-subunit mini-rings. Presumably because of their favourable rotational symmetry, the 12-subunit mini-rings were mostly organized into 2D arrays, as reported by Krupka and co-workers.

Due to the low resolution (3.6 Å) of the VmFtsA$^{1–396}$–VmFtsN$^{1–29}$ co-crystal structure (Supplementary Table 1), we could not unambiguously interpret the electron density map representing about seven or eight amino acids of the VmFtsN$^{1–29}$ peptide. We therefore confirmed the location of the VmFtsN$^{1–29}$ binding site in VmFtsA$^{1–396}$ using hydrogen deuterium exchange mass spectrometry (HDX-MS; Fig. 3c). At a threefold molar excess (30 μM) of VmFtsN$^{1–29}$ over VmFtsA$^{1–396}$, only helix 2 located in the IC domain of FtsA showed notably reduced deuterium incorporation (lower mass differential) compared with free VmFtsA$^{1–396}$ (Fig. 3c, top left). This is in agreement with VmFtsN$^{1–29}$ binding across the IC domain as seen in the co-crystal structure (Fig. 3d). FtsA peptides in filament interfaces were also protected at a tenfold molar excess (100 μM) of VmFtsN$^{1–29}$; again, most probably indicating that binding of the cytoplasmic FtsN peptide to FtsA facilitates filament formation (Fig. 3c).

As proposed previously[22], the FtsA–FtsN interaction is reminiscent of that between PilM and PilN, two proteins involved in type IV pilus formation[39]. PilM, which also has a IC subdomain, is structurally related to FtsA, and PilN, similar to FtsN, is a bitopic membrane protein with a short cytoplasmic tail comprising about 30 amino acids[39]. Both FtsN and PilN bind in the IA–IC interdomain cleft (using FtsA domain nomenclature for PilM) but use different binding modes (Extended Data Fig. 3c). PilN makes extensive contacts with the IA domain of PilM. FtsN binds further down in the cleft, predominantly contacting the IC domain of FtsA.

To try to assign the VmFtsN$^{1–29}$ peptide sequence in the VmFtsA$^{1–396}$–VmFtsN$^{1–29}$ co-crystal structure (PDB 7Q6I), we expected the N-terminal half of VmFtsN$^{1–29}$ to interact with FtsA based on the in vivo geometry, where FtsA binds to the cell membrane through its C-terminal amphipathic helix. The globular domain of FtsA was reported to be several nanometres away from the inner membrane in *E. coli*[40]. The C-terminal half of the VmFtsN$^{1–29}$ peptide would be confined to the proximity of the inner membrane as it is linked to the transmembrane helix in the full-length FtsN protein (Extended Data Fig. 2a). Amino acids M1–R8 of VmFtsN$^{1–29}$ provided the best fit for the density with reasonable chemistry—that is, several hydrogen bonds to FtsA and a hydrophobic pocket accommodating the central tyrosine (Y6) in the sequence stretch

Fig. 2 | EcFtsA forms antiparallel double filaments following binding of EcFtsN$^{1–32}$. a, Negative-stain electron micrographs of EcFtsA mutants on supported lipid monolayers with increasing concentrations of EcFtsN$^{1–32}$. EcFtsA forms mini-rings in the absence of FtsN peptide, as described previously[37]. With increasing EcFtsN$^{1–32}$ concentrations, EcFtsA forms fewer mini-rings and more double filaments. Introduction of the G50E, E124A, I143L and R286W mutations into EcFtsA facilitates filament formation at lower concentrations of EcFtsN$^{1–32}$. See also Fig. 1c and Supplementary Table 2. At least two independent grids were examined per condition. Scale bar, 20 nm. WT, wild type. **b**, SPR equilibrium response titration of EcFtsN$^{1–32}$ binding to immobilized EcFtsA (blue) or EcFtsA$^{1–405}$ (red). EcFtsN$^{1–32}$ has micromolar affinity for both FtsA proteins. RU, resonance units. **c**, EcFtsA$^{1–405}$ titration into EcFtsN$^{1–32}$-C–Atto 495. Data were fitted using a two-step model, with transitions being indicative of FtsN binding and polymerization (**d**). A representative triplicate is shown. The K_d values are given as the mean ± s.e.m. from five independent experiments. **d**, Weight-averaged sedimentation coefficients of a EcFtsA$^{1–405}$ titration into fluorescently labelled EcFtsN$^{1–32}$-C–Atto 495 by FDS–AUC show that EcFtsN$^{1–32}$ is part of higher-order FtsA polymers. Data were fitted to a two-step model, recapitulating the fluorescence polarization data in **c**. **e**, Co-pelleting assay of EcFtsN$^{1–32}$ titrated into EcFtsA$^{1–405}$ indicates that EcFtsN$^{1–32}$ induces FtsA polymerization (top). Data are the mean ± s.d. (black lines) of technical duplicates (white dots). A representative SDS–PAGE gel is shown (bottom). P, pellet; and S, supernatant. **f**, EcFtsA and EcFtsN$^{1–32}$ form double filaments on lipid monolayers as determined by cryo-EM (top). Inset: magnified view of the region in the white box. The antiparallel arrangement of the observed double filaments was confirmed by 2D classification (bottom left). A computed 2D projection from the VmFtsA double-filament crystal structure (PDB 7Q6F) is shown for comparison. Two independent grids were examined. Data were collected on one grid. Scale bars, 50 nm (main image, top), 10 nm (inset, top), 5 nm (2D class averages, bottom). **g**, The lateral interface mutant EcFtsA^{M96E,R153D}, designed based on the VmFtsA crystal structure (PBD 7Q6F) (schematic on the right), is deficient in FtsN$^{1–32}$-dependent double-filament formation, as determined by negative-stain electron microscopy on a supported lipid monolayer. Two independent grids were examined per condition. Insets: magnified views of the regions in the white boxes. Scale bars, 50 nm (main images) and 20 nm (insets).

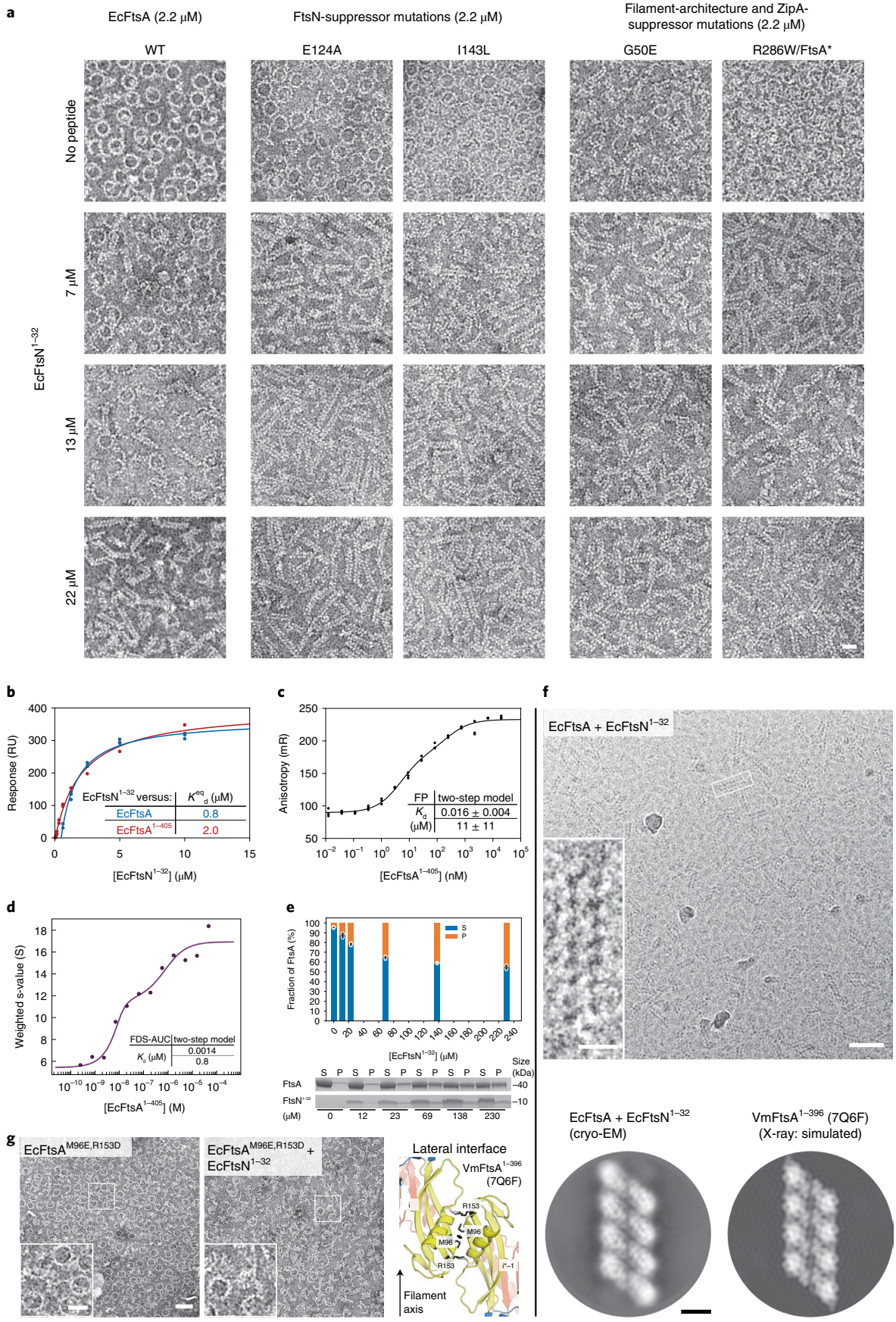
a
EcFtsA (2.2 μM)
FtsN-suppressor mutations (2.2 μM)
Filament-architecture and ZipA-suppressor mutations (2.2 μM)
WT
E124A
I143L
G50E
R286W/FtsA*
No peptide
7 μM
13 μM
22 μM
EcFtsN1–32
b
Response (RU)
EcFtsN1–32 versus: Keq d (μM)
EcFtsA 0.8
EcFtsA1–405 2.0
[EcFtsN1–32] (μM)
c
Anisotropy (mR)
FP two-step model
Kd (μM) 0.016 ± 0.004
11 ± 11
[EcFtsA1–405] (nM)
d
Weighted s-value (S)
FDS-AUC two-step model
Kd (μM) 0.0014
0.8
[EcFtsA1–405] (M)
e
Fraction of FtsA (%)
S
P
[EcFtsN1–32] (μM)
Size (kDa)
FtsA
FtsN1–32
(μM)
0
12
23
69
138
230
f
EcFtsA + EcFtsN1–32
EcFtsA + EcFtsN1–32 (cryo-EM)
VmFtsA1–396 (7Q6F) (X-ray: simulated)
g
EcFtsAM96E,R153D
EcFtsAM96E,R153D + EcFtsN1–32
Lateral interface
VmFtsA1–396 (7Q6F)
R153
M96
Filament axis

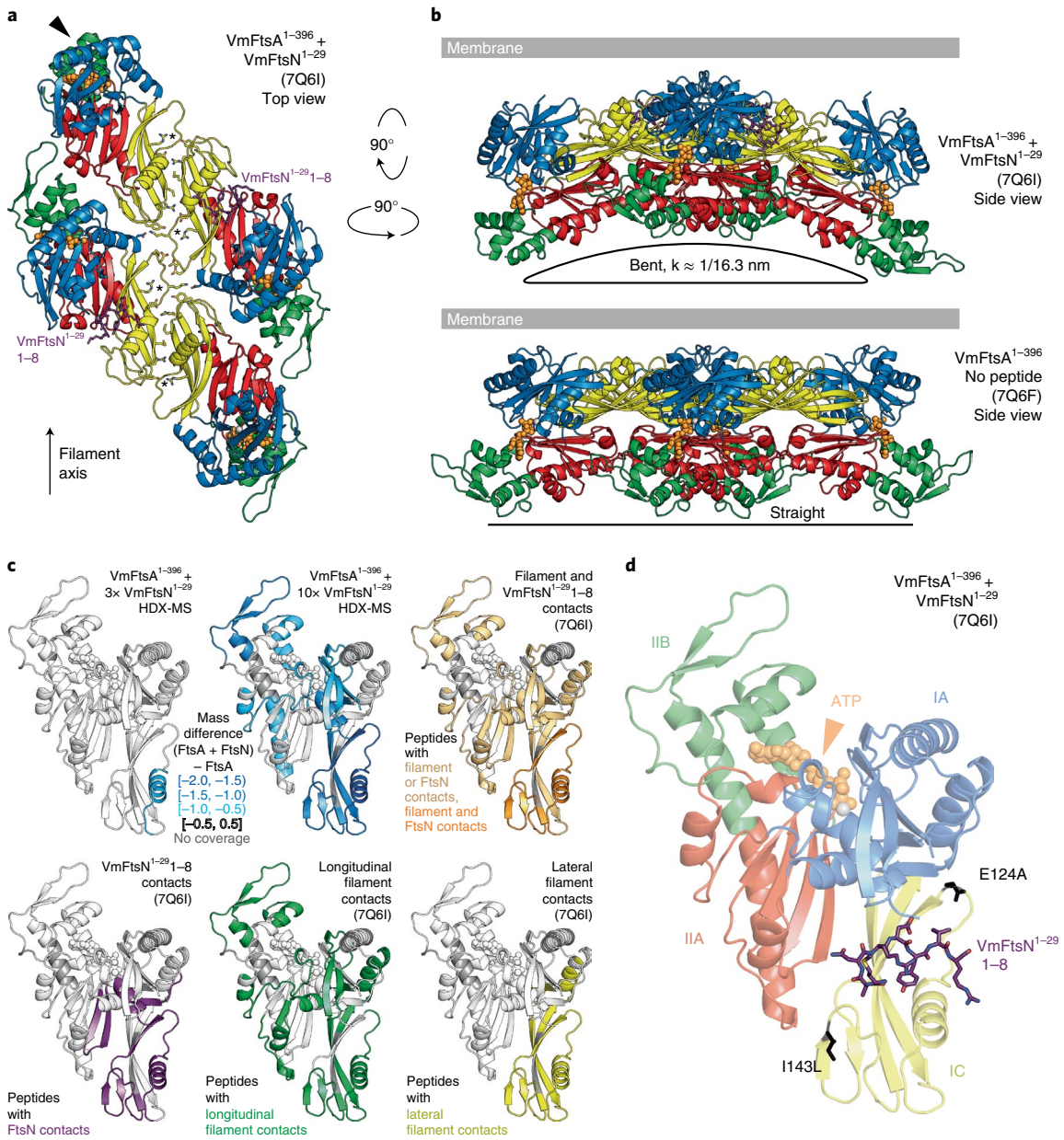

Fig. 3 | VmFtsA$^{1-396}$ and VmFtsN$^{1-29}$ crystallize as short bent double filaments. a, The 16 FtsA monomers in the asymmetric unit of the co-crystal structure are organized into short, antiparallel and curved tetramers (see also Supplementary Video 1). Top view of a representative tetramer (which requires crystal symmetry to be applied to the PDB coordinates) from the membrane-proximal side. Residues 1–8 of VmFtsN$^{1-29}$ (purple sticks) are present in the closed subunit of each protofilament. The IC domains are tilted against each other compared with the VmFtsA$^{1-396}$ double-filament structure (PDB 7Q6F), presumably destabilizing the R91–Y139 interaction (asterisks) in the lateral interface. The IIB domain of the top-left monomer (chain D) is partially disordered (arrowhead). **b**, A comparison of the side views of the crystal structures of PDB 7Q6I (top) and 7Q6F (bottom) illustrates that the 7Q6I tetramer is bent along the filament axis. k, curvature. **c**, HDX-MS analysis of VmFtsA$^{1-396}$ with a three- (30 µM; top left) or tenfold molar excess (100 µM; top middle) of VmFtsN$^{1-29}$, confirming that VmFtsN$^{1-29}$ binds in the IA–IC interdomain cleft of FtsA. Peptides that are protected in the presence of VmFtsN$^{1-29}$ (slower exchange of hydrogen for deuterium) are highlighted in blue. Presumably because high concentrations of VmFtsN$^{1-29}$ induce polymerization of VmFtsA$^{1-396}$ (Extended Data Fig. 2d,e), peptides mapping to the filament interfaces are protected as well. For orientation, peptides are coloured according to their involvement in different interfaces of the VmFtsA$^{1-396}$–VmFtsN$^{1-29}$ co-polymer (PDB 7Q6I). **d**, Residues 1–8 of VmFtsN$^{1-29}$ bind in the IA–IC interdomain cleft of VmFtsA$^{1-396}$. The positions of the FtsN-suppressor mutations E124A[27] and I143L[16] are shown in black.

(Extended Data Fig. 3d, top). This model also implies a central position of D5 within the FtsA–FtsN interaction site that could point to a mechanism by which the D5N mutation impairs double-filament formation (Extended Data Fig. 2h and Extended Data Fig. 3d, top). In that case, FtsN^{D5N} would not be able to bridge the IA and IC domains of FtsA. We also studied the VmFtsA$^{1-396}$–VmFtsN$^{1-29}$ interaction using nuclear magnetic resonance (NMR) spectroscopy. We assigned the peptide backbone of GG-VmFtsN$^{2-29}$, a VmFtsN$^{1-29}$ construct in which two glycine residues replace the N-terminal methionine (Extended Data Fig. 3e). Next, we analysed peak broadening (reduction in peak intensity due to the slower tumbling rate of the FtsA-bound GG-VmFtsN$^{2-29}$ peptide) following the

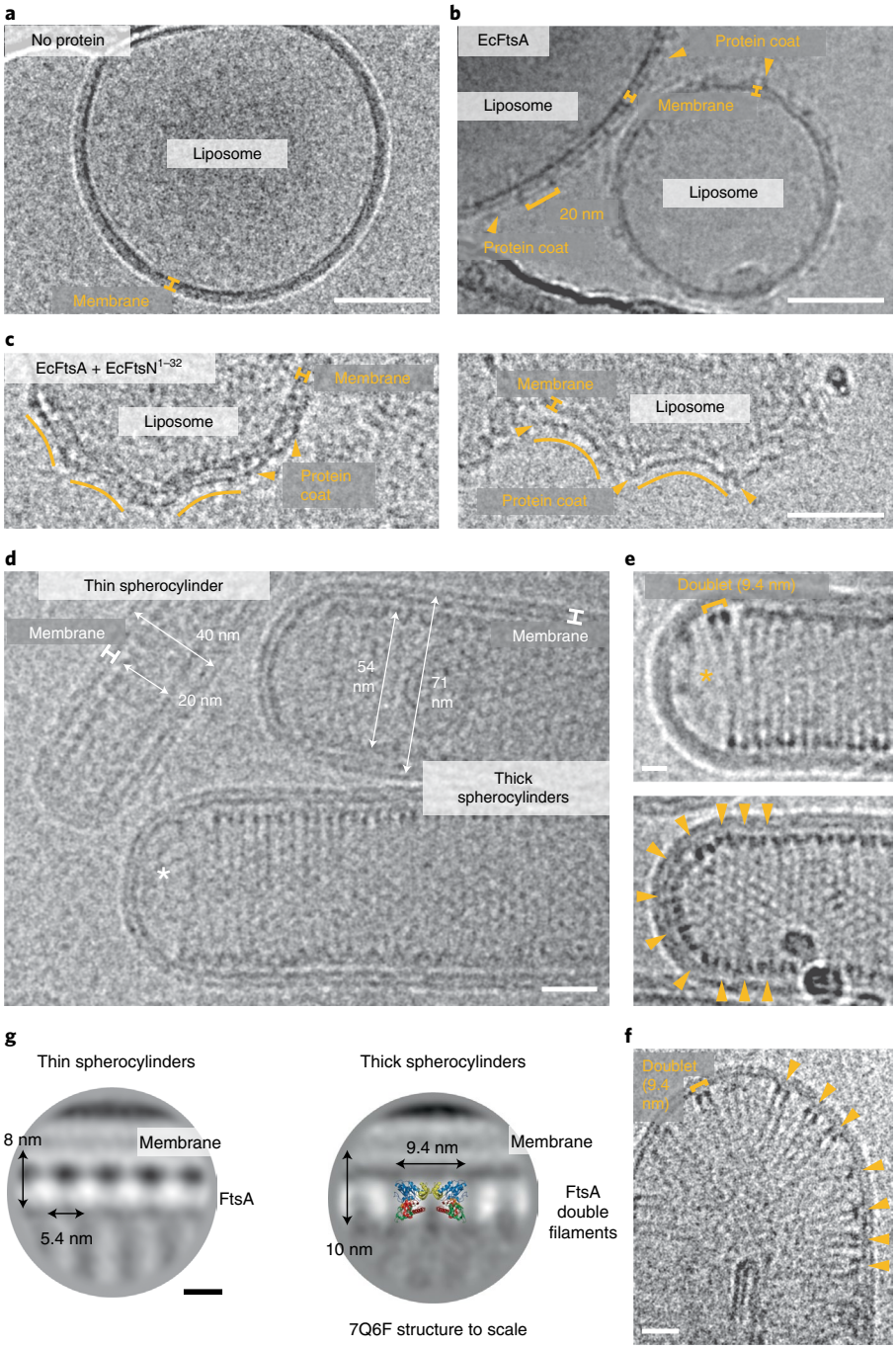

Fig. 4 | EcFtsA–FtsN$^{1-32}$ double filaments orient inside liposomes. a, Cryo-EM micrograph showing a spherical liposome with no proteins added. The carbon edge of the grid is visible at the top of the image. **b**, Cryo-EM micrograph of liposomes with EcFtsA (arrowheads) bound to the outside. Liposomes show no indentations. The protein coat shows a 20-nm repeat, indicating the presence of EcFtsA mini-rings (see also Extended Data Fig. 3b). The carbon edge of the grid is visible at the bottom left of the image. **c**, Cryo-EM micrographs of two different liposomes with EcFtsA–FtsN$^{1-32}$ filaments (arrowheads) bound to the outside. Indentations in the liposomes can be observed. See Salje et al.[4] for a comparison with MreB filaments added to liposomes. **a**–**c**, Scale bars, 50 nm. **d**, Co-encapsulation of EcFtsA and EcFtsN$^{1-32}$ in liposomes produces thin and thick protein-filled spherocylinders (rods) with diameters of approximately 40 nm and 70 nm, respectively. EcFtsA–FtsN$^{1-32}$ filaments align with the short axis of the spherocylinders. There are no filaments in the hemisphere of a thick spherocylinder (asterisk). See Hussain et al.[34] for a comparison with MreB filaments encapsulated into liposomes. Scale bar, 20 nm. **e**, Cryo-EM micrographs of EcFtsA–FtsN$^{1-32}$ double filaments in thick spherocylinders. EcFtsA–FtsN$^{1-32}$ double filaments align with the short axis of thick spherocylinders (top); there are no filaments in the hemisphere of the spherocylinder (asterisk). EcFtsA–FtsN$^{1-32}$ double filaments align with the short axis in the cylindrical part of the spherocylinder but are randomly oriented in the hemisphere (arrowheads; bottom). Scale bar, 10 nm. **f**, Liposome with a few EcFtsA–FtsN$^{1-32}$ double filaments inside. EcFtsA–FtsN$^{1-32}$ double filaments are randomly oriented in the semi-circular part of the liposome but are more aligned in the cylindrical part (arrowheads). Scale bar, 20 nm. **a**–**f**, At least two independently prepared grids were examined per condition. **g**, Two-dimensional class averages of FtsA membrane attachment sites in thin (left) and thick (right) spherocylinders. EcFtsA–FtsN$^{1-32}$ are organized into single protofilaments in thin spherocylinders. Thick spherocylinders contain EcFtsA–FtsN$^{1-32}$ double filaments. The end view of the VmFtsA$^{1-396}$ double filament structure (PDB 7Q6F) is shown to scale (right). Scale bar, 5 nm.

addition of equimolar amounts of VmFtsA$^{1–396}$ (Extended Data Fig. 3f). Intensity reduction was most prominent in the stretch of the amino acids Y6–G10 (Extended Data Fig. 3f), suggesting a slightly shifted binding motif compared with our density-based assignment (M1–R8; Extended Data Fig. 3d). We were unable to generate a good fit of these residues into the electron density map of the VmFtsA$^{1–396}$–VmFtsN$^{1–29}$ co-crystal structure. For technical reasons, the NMR experiments were carried out at pH 6.0, whereas the binding experiments were performed at pH 7.7 and crystallization was achieved at pH 8.5.

FtsA double filaments adopt a negative Gaussian curvature. Based on the observation that VmFtsA$^{1–396}$–VmFtsN$^{1–29}$ double filaments were curved in the co-crystal structure (Fig. 3b), we hypothesized that the intrinsic curvature preference observed for MreB double filaments might also be a feature of FtsA–FtsN double filaments[4,34]. The curvature preference of MreB filaments has been proposed to enable a curvature-sensing mechanism that allows them to robustly align in cells with the axis of highest principal curvature, which corresponds to the short axis of rod-shaped bacteria such as *E. coli* and *B. subtilis*[34,35].

To investigate the curvature preference of FtsA filaments, we added EcFtsA–FtsN$^{1–32}$ to pre-formed liposomes made from *E. coli* polar lipid extract. Liposomes are typically round or oval in the absence of proteins (Fig. 4a). Liposomes coated with EcFtsA alone are also round or oval (Fig. 4b). The FtsA coat showed a 20-nm repeat, indicating the presence of FtsA mini-rings[37] (see also Extended Data Fig. 3b). In contrast, liposomes coated with EcFtsA–FtsN$^{1–32}$ double filaments showed membrane indentations with a negative Gaussian curvature (Fig. 4c). Previously published images of MreB double filaments bound to the outside of liposomes have demonstrated a remarkably similar binding mode[4,33]. To better match the geometry inside an *E. coli* cell, we then encapsulated EcFtsA–FtsN$^{1–32}$ double filaments in liposomes. Protein-filled liposomes were spherocylindrical (rod-shaped) or had spherocylindrical protrusions (Fig. 4d). The spherocylinders were either approximately 40 nm or 70 nm in diameter. The thicker spherocylinders contained tightly packed EcFtsA–FtsN$^{1–32}$ double filaments that were aligned with the short axis in the cylindrical section (Fig. 4d,e). Similar filament arrangements of MreB filaments inside liposomes can be seen in previously published images[34]. EcFtsA–FtsN$^{1–32}$ filaments were regularly absent in the hemispheres (poles) of thick spherocylinders (Fig. 4d,e). If filaments were present in the hemispheres, they showed random angular orientations (Fig. 4e, bottom). Although infrequent, we obtained liposomes containing only a few EcFtsA–FtsN$^{1–32}$ double filaments (Fig. 4f). The filaments were again distributed randomly in spherical sections of the liposomes but aligned with the short axis of the liposomes in more cylindrical sections. We performed 2D averaging and image classification focussed on the membrane attachment sites of the FtsA filaments in thin and thick spherocylinders. Class averages clearly illustrated the different organization of FtsA filaments in thin and thick spherocylinders (Fig. 4g). In the thin spherocylinders, FtsA was organized into bent single protofilaments (Fig. 4g, left). However, FtsA formed bent double filaments in the thick spherocylinders, which was apparent by superposition of the VmFtsA$^{1–396}$ double-filament crystal structure (PDB 7Q6F) onto the 2D class average (Fig. 4g, right).

***E. coli* FtsA forms antiparallel double filaments in vivo.** To validate our in vitro findings, we investigated the formation of FtsA double filaments in vivo using site-specific cysteine cross-linking in *E. coli*. We inserted a *neoR* marker downstream of *lpxC* for positive selection (Extended Data Fig. 4a). For visualization via western blotting, we introduced a 3×haemagglutinin (HA) tag (comprising 40 amino acids including linkers) into the H7–S12 loop of FtsA[41]. The cysteine mutations for in vivo site-specific cross-linking were designed based on the crystal structure of VmFtsA$^{1–396}$ double filaments (PDB 7Q6F; Fig. 5a, see also Extended Data Fig. 5a). Mutant strains showed no growth defects and no elongated cells compared with the MG1655 parent strain (Extended Data Fig. 4b–d).

In this way, we generated the FtsA double cysteine-mutant strains *ftsA*$^{3×HA,P98C,S118C}$ and *ftsA*$^{3×HA,E199C,S252C}$, which probe the lateral FtsA$_i$–FtsA$_{i^*-1}$ and the longitudinal FtsA$_i$–FtsA$_{i\pm1}$ interfaces of the FtsA double filament, respectively (Fig. 5b). *E. coli* cells in the exponential phase (optical density at 600 nm (OD_{600}) = 0.2–0.4) were treated with bismaleimidoethane (BMOE). BMOE enters living *E. coli* cells and rapidly cross-links closely spaced thiols such as cysteine side chains in vivo. FtsA species were visualized using western blotting against the 3×HA tag in FtsA (Fig. 5c). We detected efficient formation of cross-linked FtsA dimers for both the *ftsA*$^{3×HA,P98C,S118C}$ and *ftsA*$^{3×HA,E199C,S252C}$ double mutants but only weak background signal spread across multiple species in the single cysteine-mutant controls (Fig. 5c; see also Extended Data Fig. 5a). We also detected higher-order polymers for the *ftsA*$^{3×HA,E199C,S252C}$ mutant, presumably because the open symmetry of the longitudinal filament contact allows for more than two FtsA monomers to be cross-linked through chaining.

To probe the lateral association further, we generated two additional FtsA single cysteine-mutant strains, *ftsA*$^{3×HA,D123C}$ and *ftsA*$^{3×HA,Q155C}$, which probe the lateral FtsA$_i$–FtsA$_{i^*}$ and FtsA$_i$–FtsA$_{i^*-1}$ interfaces of the FtsA double filament, respectively (Fig. 5d). These single-cysteine mutants may cross-link to their symmetry mates because of the local C2 symmetry in each of the two lateral filament interfaces. However, the C_β–C_β distances in the VmFtsA double-filament structure of 3.7 Å for FtsA$^{3×HA,D123C}$ and 12.6 Å for FtsA$^{3×HA,Q155C}$ indicated that cross-linking with BMOE

Fig. 5 | FtsA forms antiparallel double filaments in vivo. a, Domain architecture of EcFtsA (the amino acids positions are the same for VmFtsA). Positions of cysteine mutations and the 3×HA tag (comprising 40 amino acids including linkers, grey) are indicated. Striped areas correspond to disordered residues in the VmFtsA$^{1–396}$ double-filament structure (PDB 7Q6F). **b**, The cysteine-mutation pairs FtsA$^{3×HA,P98C,S118C}$ and FtsA$^{3×HA,E199C,S252C}$ probing the lateral and longitudinal filament interfaces, respectively, are highlighted on the VmFtsA double-filament structure (PDB 7Q6F). The C_β–C_β distances between the cysteine residues and the position of the 3×HA tag are indicated. Inset: the probed interfaces in the context of the double filament. SW, sandwich fusion. **c**, Western blot analysis (using anti-HA–HRP) of cell lysates from FtsA cysteine mutant *E. coli* strains after in vivo cysteine cross-linking (+BMOE; left) and without cross-linking (−BMOE; right). Signal for covalent FtsA dimers can be detected for both double mutants. For *ftsA*$^{3×HA,E199C,S252C}$, higher-order oligomers can be detected because of the open symmetry of the longitudinal contact, which leads to chaining. Similar results were achieved in biological triplicates. WT, wild type. **d**, Cysteine mutations *ftsA*$^{3×HA,D123C}$ and *ftsA*$^{3×HA,Q155C}$ probing the lateral FtsA$_i$–FtsA$_{i^*}$ and FtsA$_i$–FtsA$_{i^*-1}$ filament interfaces, respectively, are highlighted on the VmFtsA double-filament structure (PDB 7Q6F). The C_β–C_β distances between C residues and the position of the 3×HA tag are indicated. Both single cysteine mutations utilize the local C2 symmetry of the respective lateral interface for cross-linking. Inset: probed interfaces in the context of the double filament. **e**, Western blot analysis (using anti-HA–HRP) of cell lysates from FtsA cysteine-mutant *E. coli* strains after in vivo cysteine cross-linking with and without using thiol-directed cross-linkers of different lengths—that is, dBBr, BMB, BMH and BMOE. Signal for a FtsA dimer can be detected after using dBBr and, to a lesser extent, BMOE cross-linking in the *ftsA*$^{3×HA,D123C}$ mutant (left). For the *ftsA*$^{3×HA,Q155C}$ mutation (right), FtsA dimers can be detected after cross-linking with BMB or BMH but not with BMOE. Similar results were achieved in biological duplicates. **f**, Structures and estimated cross-linking distances for the cross-linkers used in this study.

with an expected cross-linking distance of about 8 Å might be inefficient, which prompted us to try thiol-directed cross-linkers of different lengths (Fig. 5f). The *ftsA*$^{3\times HA,D123C}$ mutant showed more efficient cross-linking of FtsA using dibromobimane (dBBr) than BMOE (Fig. 5e, left). In the case of the *ftsA*$^{3\times HA,Q155C}$ mutant, BMOE cross-linking did not lead to efficient formation of covalent FtsA dimers, whereas treatment with the longer maleimide cross-linkers 1,4-bismaleimidobutane (BMB) and bismaleimidohexane (BMH) did (Fig. 5e, right). Together, our data strongly suggest that FtsA forms protofilaments in cells and that these protofilaments are further arranged into antiparallel double filaments, as suggested by the crystal structure of VmFtsA$^{1-396}$ (PDB 7Q6F).

Conclusion

We report that FtsA polymerizes to form antiparallel double filaments in *E. coli* and found that filament formation is induced through binding to the cytoplasmic tail of FtsN in vitro. The only other actin-like protein known to polymerize into antiparallel

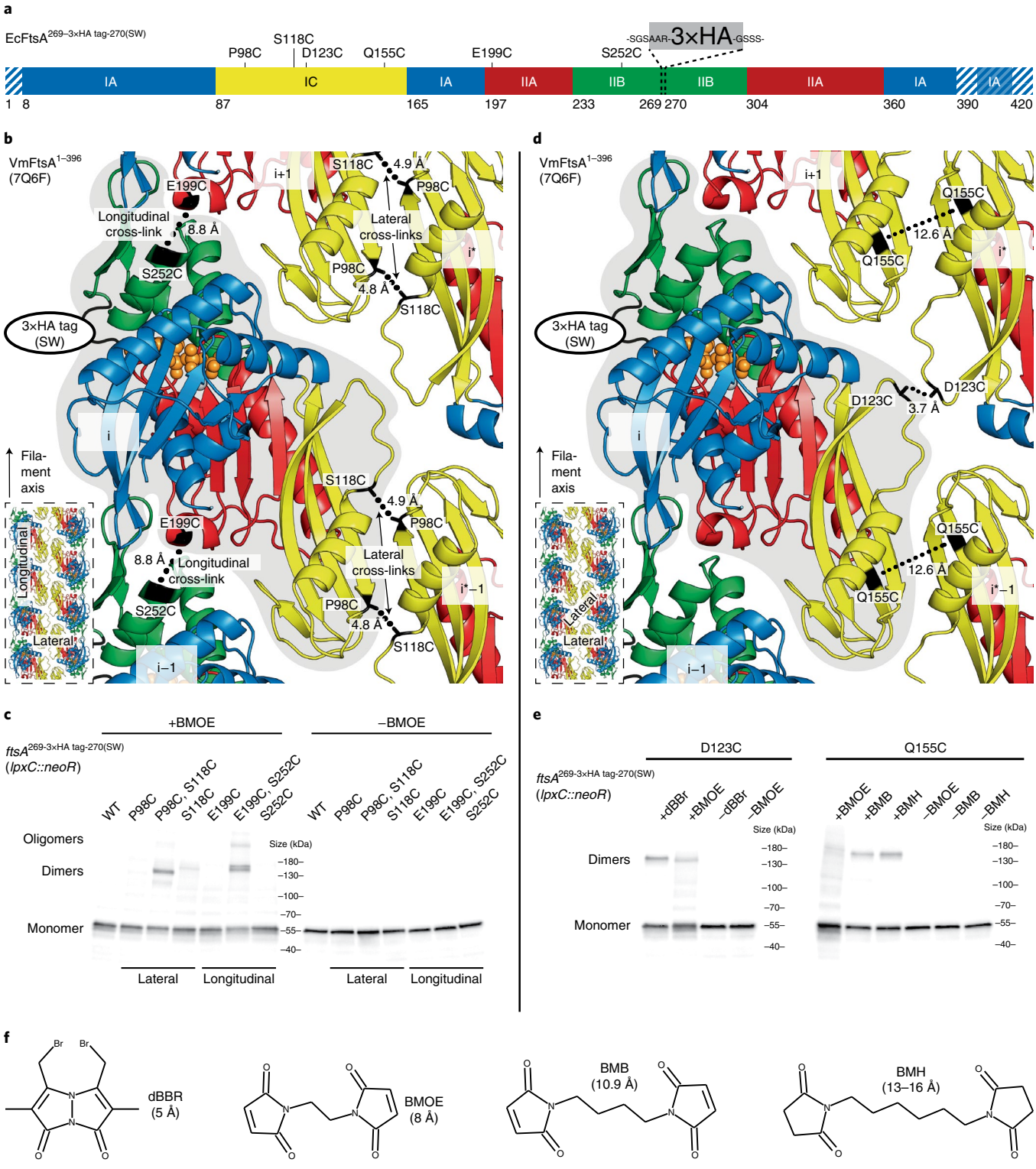

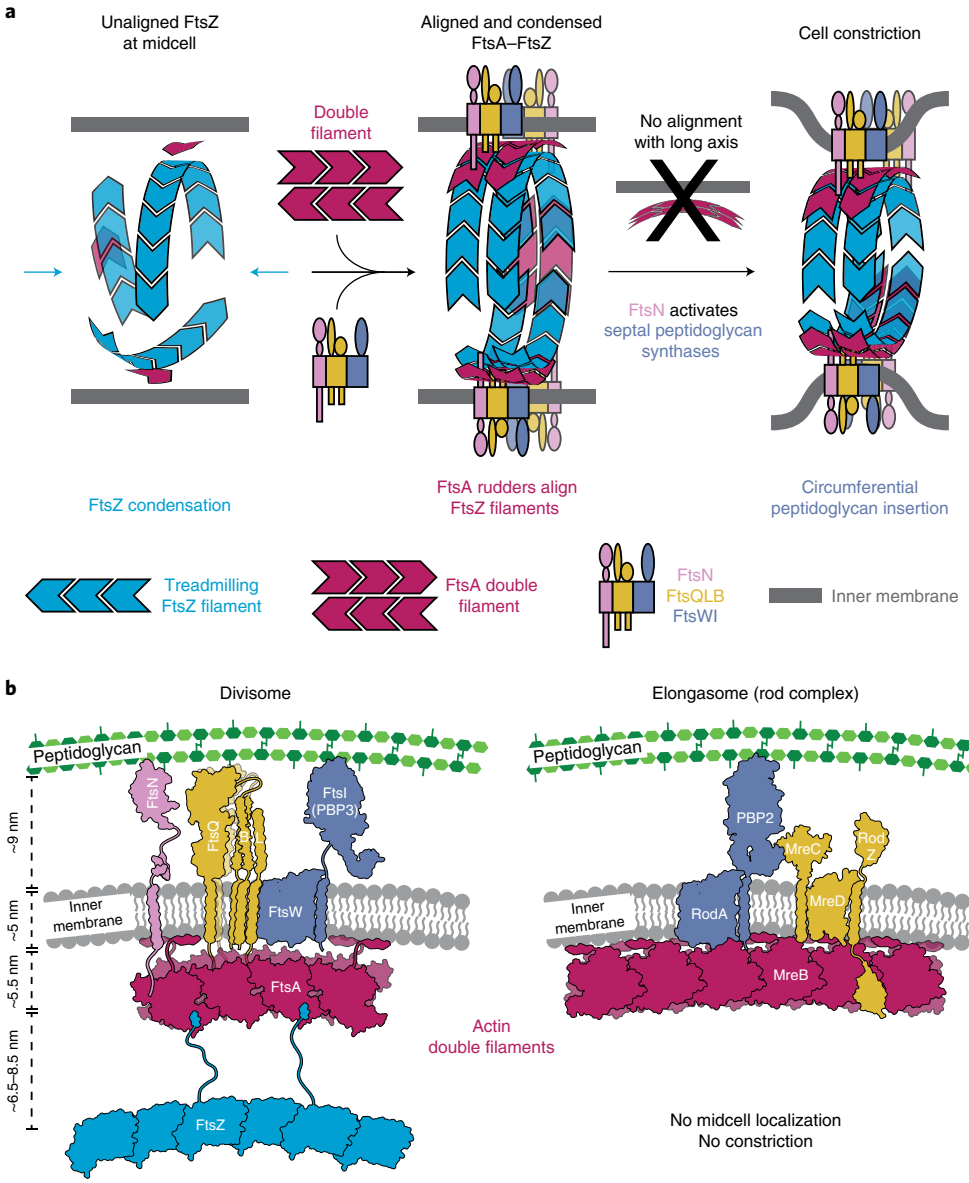

Fig. 6 | Model for septal peptidoglycan synthesis and cell constriction. a, Logical steps towards a divisome primed for curvature-guided septal peptidoglycan synthesis. The temporal order of events remains to be determined. FtsZ filaments recruited to the midcell are unaligned (left). Downstream divisome proteins are recruited and condensed into the narrow midcell plane by treadmilling FtsZ filaments that themselves will also be aligned through their interaction with curvature-sensing FtsA filaments (middle). Condensed complexes are aligned with the short axis of the cell by FtsA double filaments because of their curvature-sensing mechanism, which we propose here they share with MreB. Finally, FtsZ filaments distribute divisome components via treadmilling and might thereby reinforce their alignment with the short axis of the cell. FtsN is required for the formation of FtsA double filaments and activation of septal peptidoglycan synthases. By coordinating both activities across the inner membrane, FtsN might constitute a synchronizing activation switch for the divisome, which allows circumferential synthesis of septal peptidoglycan through the alignment activity and at the same time cell constriction to commence through the activation of peptidoglycan synthesis (right). **b**, Schematic overview of core components of the divisome and elongasome highlighting the evolutionary relationship between the two complexes. We propose here that both complexes utilize the curvature-sensing properties of their cytoplasmic actin double-filament scaffolds (red) to direct peptidoglycan synthesis around the circumference of the cell. The bipartite peptidoglycan synthases (FtsWI and RodA–PBP2, purple) are connected to the actin double filaments via integral membrane proteins that serve as structural and regulatory subunits (yellow), or potentially even directly. Unlike the elongasome, the divisome in FtsN possesses an additional regulatory subunit that might be necessary given that cell division is regulated during the cell cycle. FtsZ is absent in the elongasome. FtsZ localizes the divisome and its activities to the midcell and probably more importantly into a narrow plane, an activity that is neither required nor desired in the elongasome.

double filaments is MreB, the actin homologue in the elongasome, which serves as a rudder to guide peptidoglycan insertion in the cell wall during growth[31,33,34]. We observed that FtsA–FtsN filaments preferentially bind surfaces of negative Gaussian curvature in and on liposomes, as do MreB double filaments[4,33,34] (Fig. 4). We therefore propose that MreB and FtsA have a common curvature-sensing mechanism. Finally, we devised a model for curvature-guided cell constriction by FtsA–FtsN double filaments, which align the direction of the glycan strand synthesis activity of the divisome with the circumference of the cell (Fig. 6a).

In our model we define three phases in divisome assembly and maturation. Unaligned FtsZ filaments are present at the midcell in phase 1, a fully assembled divisome aligns with the short axis of the cell in phase 2 and the divisome is fully activated in phase 3, synthesizing septal peptidoglycan and enabling cell constriction (Fig. 6a). We note that the temporal order of individual recruitment and activation events during divisome maturation remains largely unknown and could be informed by in vivo single-molecule imaging of FtsA. FtsZ filaments are present at the midcell, presumably to determine the division plane, but are unaligned in the absence of an alignment mechanism (Fig. 6a, left). After recruitment of divisome proteins and Z-ring condensation[10,11], which has previously been proposed to be driven by a FtsA mini-ring-to-double filament transition[32,37], FtsN-induced FtsA double filaments align themselves and other divisome components with the short axis of the cell. This process might be aided by FtsZ treadmilling, which could provide a long-range distribution mechanism[7,8,42] (Fig. 6a, middle).

We propose that curvature-sensing FtsA double filaments provide a solution to the FtsZ alignment problem of how FtsZ filaments align with the short cell axis during division[43]. Consistent with this, the fraction of directionally treadmilling FtsZ filaments decreases in a Δ*ftsA* strain of *B. subtilis*[10]. We hypothesize that FtsA double filaments and treadmilling FtsZ filaments align and evenly distribute divisome components in the narrow division plane. Most importantly, this could restrict movement of FtsWI—which is the bipartite peptidoglycan synthase of the divisome—in such a way that cell-constricting septal peptidoglycan synthesis follows the circumference of the cell (Fig. 6a, right). FtsN might function as an activation switch of the divisome by coordinating activities of FtsA and FtsWI. A more direct interaction between FtsA and FtsW has also been recently proposed[44].

We found that the short cytoplasmic tail of FtsN promotes the formation of FtsA double filaments (Fig. 2a,d,e), which adds to previous evidence reporting that FtsA can form different polymers[30,32,37]. Importantly, our structural data reveal that the FtsA double filament is compatible with FtsN binding. Double-filament formation also positions the FtsA IC domain close to the inner membrane (Extended Data Fig. 1c), which might facilitate binding of divisome components such as FtsQ[24].

Together with recent reports establishing FtsWI[45] and RodA–PBP2 (refs. [46,47]) as bipartite peptidoglycan synthases, our data showing the similarities between FtsA and MreB double filaments strengthen the previously proposed evolutionary relationships between the divisome and elongasome[2] (Fig. 6b). MreB has been implicated in the organization of cell division in *Chlamydia*[48]—one of the few bacteria that lack FtsZ—which further suggests that the divisome and elongasome share some basic functions.

Which of the many functions of FtsZ make it the early organizer of the divisome but are not required in the elongasome? Our model suggests that FtsZ is the long-range organizer of the division site, which ensures that septal peptidoglycan synthases only function in a single division plane and are evenly distributed around the circumference of the cell. FtsA aligns the peptidoglycan synthases with the orientation of the division ring so that septal peptidoglycan glycan synthesis mediated by the divisome goes around the circumference of the ring.

Future studies will need to pinpoint at which point during cell division FtsA double filaments form. The difference in interaction partners between monomeric and polymeric FtsA as well as how they influence each other will need to be investigated concomitantly. These studies will deepen our understanding of the central role of FtsA polymerization in FtsZ-based cell division and bring us closer to in vitro reconstitution of bacterial cell division.

Methods

Expression plasmids. Expression plasmids (Supplementary Table 3) were cloned using NEBuilder HiFi DNA assembly mix (NEB). Either *E. coli* MAX efficiency DH5α (ThermoFisher) or C41(DE3) cells (Lucigen or Sigma) were used for plasmid propagation and protein expression, respectively. The plasmid sequences are provided in Supplementary Data 1.

Protein expression and purification. The sequences of all proteins used in this study are listed in Supplementary Table 4. Purifications were carried out at 4–6 °C unless stated otherwise. Buffers were prepared in Millipore water, pH-adjusted at room temperature (RT) and filtered through a 0.22-µm PES filter.

GST–SENP1. GST–SENP1 was expressed in C41(DE3) cells cultured at 37 °C in 2×TY medium supplemented with 100 µg ml^{-1} ampicillin. The cells were induced with 0.5 mM isopropyl-β-D-thiogalactoside (IPTG) at OD_{600} = 0.6–0.8, cultured overnight at 18 °C and harvested by centrifugation. The cells were lysed in buffer SA (50 mM Tris–HCl, 150 mM NaCl, 2 mM tris(2-carboxyethyl)phosphine (TCEP), 1 mM EDTA and 5% glycerol, pH 8.5), supplemented with DNase, RNase and cOmplete EDTA-free protease inhibitor cocktail (Roche), using a cell disruptor at 25 kpsi (Constant Systems). The lysate was centrifuged at 100,000*g* for 30 min at 4 °C. The supernatant was added to Glutathione Sepharose 4B beads (Cytiva) and incubated for 2 h at 4 °C. The beads were thoroughly washed in buffer SA, followed by buffer SA with 500 mM NaCl and again buffer SA. The protein was eluted in buffer SA with 10 mM reduced glutathione. The peak fractions were concentrated using a Vivaspin 20 concentrator (molecular weight cut-off (MWCO) of 30 kDa, Sartorius). The protein was further purified by size-exclusion chromatography on a HiLoad 26/600 Superdex 200 pg column (Cytiva) equilibrated in buffer SEC-S (50 mM Tris–HCl, 50 mM NaCl, 5 mM TCEP, 1 mM EDTA, 1 mM NaN_3 and 5% glycerol, pH 8.0). The peak fractions were concentrated to approximately 15–20 mg ml^{-1}, frozen in aliquots and stored at −80 °C.

6H-TEV protease. 6H-TEV protease was expressed in C41(DE3) cells cultured at 37 °C in 2×TY medium supplemented with 30 µg ml^{-1} kanamycin. The cells were induced with 1 mM IPTG at OD_{600} = 0.6–0.8, cultured overnight at 19 °C and harvested by centrifugation. The cells were lysed in TEV lysis buffer (20 mM Tris–HCl, 500 mM NaCl, 1 mM TCEP and 1 mM NaN_3, pH 8.0), supplemented with DNase and RNase, using a cell disruptor at 25 kpsi (Constant Systems). The lysate was centrifuged at 100,000*g* for 30 min at 4 °C. The supernatant was supplemented with 20 mM imidazole and loaded onto a HisTrap FF column (Cytiva). The column was washed with TEV lysis buffer supplemented with 20 mM imidazole. The protein was eluted in TEV lysis buffer with increasing concentrations of imidazole, concentrated using Vivaspin 20 concentrators (MWCO of 10 kDa; Sartorius) and further purified by size-exclusion chromatography on a HiLoad 16/600 Superdex 75 pg column (Cytiva) equilibrated in TEV lysis buffer. The peak fractions were concentrated to 30 mg ml^{-1}, frozen in aliquots and stored at −80 °C.

Full-length FtsA. C-terminal intein-CBD-12H fusions of EcFtsA, EcFtsA^{M96E,R153D}, EcFtsA^{E124A}, EcFtsA^{I143L}, EcFtsA^{G50E}, EcFtsA^{R286W} and VmFtsA were expressed in C41(DE3) cells cultured at 37 °C in 2×TY medium supplemented with 100 µg ml^{-1} ampicillin. The cells were induced with 0.5 mM IPTG at OD_{600} = 0.8–1.0, cultured overnight at 18 °C and harvested by centrifugation. The cells were lysed in buffer LB2 (50 mM Tris–HCl, 500 mM NaCl, 5 mM TCEP, 10 mM $MgCl_2$ and 1 mM NaN_3, pH 8.0), supplemented with DNase, RNase and cOmplete EDTA-free protease inhibitor cocktail (Roche), using a cell disruptor at 25 kpsi (Constant Systems). The lysate was centrifuged at 100,000*g* for 30 min at 4 °C. The supernatant was supplemented with 50 mM imidazole and loaded onto a HisTrap HP column (Cytiva). The column was washed with buffer SEC2 (50 mM *N*-cyclohexyl-2-aminoethanesulfonic acid (CHES)–KOH, 500 mM KCl, 5 mM TCEP, 10 mM $MgCl_2$, 5% glycerol and 1 mM NaN_3, pH 9.0) supplemented with 100 mM imidazole. The protein was eluted in buffer SEC2 with increasing concentrations of imidazole and loaded onto chitin resin (NEB) packed in a XK 50/20 column (Cytiva). The column was thoroughly washed with buffer CHIT2 (buffer SEC2 with 1 mM EGTA), followed by buffer CHIT2 with 50 mM 2-mercaptoethanol (2-ME) and incubated overnight at 4 °C without flow, allowing for intein cleavage. The cleaved FtsA was eluted in buffer CHIT2 with 50 mM 2-ME, followed by buffer CHIT2, concentrated using Vivaspin 20 concentrators (MWCO of 30 kDa; Sartorius) and further purified by size-exclusion chromatography on a HiLoad 16/600 Superdex 200 pg column (Cytiva) equilibrated in buffer SEC2. The peak fractions were concentrated to 7–8 mg ml^{-1}, frozen in aliquots and stored at −80 °C. The protein mass was verified using electrospray ionization time-of-flight (ESI-TOF) mass spectrometry.

C-terminally truncated FtsA. N-terminal 6H-SUMO fusions of EcFtsA$^{1–405}$, XpFtsA$^{1–396}$ and VmFtsA$^{1–396}$ were expressed in C41(DE3) cells cultured at 37 °C in 2×TY medium supplemented with 30 µg ml^{-1} kanamycin. The cells were induced with 0.5 mM IPTG at OD_{600} = 0.8–1.0, cultured for 5 h at 37 °C (6H-SUMO–XpFtsA$^{1–396}$) or overnight at 25 °C (6H-SUMO–EcFtsA$^{1–405}$ and 6H-SUMO–VmFtsA$^{1–396}$) and harvested by centrifugation. The cells were lysed in buffer LB2, supplemented with DNase, RNase and cOmplete EDTA-free protease inhibitor cocktail (Roche), using a cell disruptor at 25 kpsi (Constant Systems). The lysate was centrifuged at 100,000*g* for 30 min at 4 °C. The supernatant was supplemented with 20 mM imidazole and loaded onto a HisTrap HP column (Cytiva).

The column was washed with buffer SEC2 containing 20 mM imidazole. The protein was eluted in buffer SEC2 with increasing concentrations of imidazole, mixed with Glutathione Sepharose 4B beads (Cytiva) and purified GST–SENP1, and incubated at 4 °C overnight. The samples were passed through a gravity flow column and concentrated using Vivaspin 20 concentrators (MWCO of 30 kDa; Sartorius). The concentrated protein was further purified by size-exclusion chromatography on a HiLoad 26/600 Superdex 200 pg column (Cytiva) equilibrated in buffer SEC2 for $EcFtsA^{1–405}$ or crystallization buffer (20 mM CHES–KOH, 100 mM KCl, 5 mM TCEP, 5 mM $MgCl_2$, 5% glycerol and 1 mM NaN_3, pH 9.0) for $XpFtsA^{1–396}$ and $VmFtsA^{1–396}$. The peak fractions were concentrated to 12–19 mg ml^{-1}, frozen in aliquots and stored at −80 °C. The protein mass was verified using ESI-TOF mass spectrometry.

Isotope-labelled $VmFtsN^{1–29}$-ENLYFQ and GG-$VmFtsN^{2–29}$. Isotope-labelled $VmFtsN^{1–29}$-TEV-lipoyl tag-6H (resulting in $VmFtsN^{1–29}$-ENLYFQ) and 6H-lipoyl tag-TEV-G-$VmFtsN^{2–29}$ (resulting in GG-$VmFtsN^{2–29}$) were expressed in C41(DE3) cells in M9 medium (6 g l^{-1} Na_2HPO_4, 3 g l^{-1} KH_2PO_4 and 0.5 g l^{-1} NaCl) supplemented with 100 µg ml^{-1} ampicillin and 1.7 g l^{-1} yeast nitrogen base without NH_4Cl and amino acids (Sigma, Y1251) at 37 °C. The culture medium was supplemented with 1 g l^{-1} $^{15}NH_4Cl$ and 4 g l^{-1} ^{13}C-glucose for ^{15}N and ^{13}C labelling, respectively. The cells were induced with 0.5 mM IPTG at OD_{600} = 0.6–0.8, cultured overnight at 25 °C and harvested by centrifugation. The cells were lysed in buffer LB5 (50 mM HEPES–KOH, 250 mM KCl and 1 mM TCEP, pH 7.7), supplemented with DNase, RNase and cOmplete EDTA-free protease inhibitor Cocktail (Roche), using a cell disruptor at 25 kpsi (Constant Systems). The lysate was centrifuged at 100,000*g* for 30 min at 4 °C. Before loading onto a HisTrap HP column (Cytiva), 20 mM imidazole was added to the supernatant. The column was washed with buffer LB5 containing 20 mM or 50 mM imidazole for $VmFtsN^{1–29}$-TEV-lipoyl tag-6H and 6H-lipoyl tag-TEV-G-$VmFtsN^{2–29}$, respectively. The proteins were eluted in buffer LB5 with increasing concentrations of imidazole, mixed with 6H-TEV protease and incubated overnight at 4 °C. Next, the samples were diluted in buffer LB5 to a final imidazole concentration of approximately 50 mM and loaded onto a HisTrap HP column equilibrated in buffer LB5 with 50 mM imidazole. The column was washed with buffer LB5 supplemented with 50 mM imidazole and the flow-through and wash fractions were concentrated using Vivaspin 15 R concentrators (MWCO of 2 kDa; HY membrane; Sartorius).

For GG-$VmFtsN^{2–29}$ only, the sample was further diluted in buffer SA2 (50 mM HEPES–KOH, 50 mM KCl and 1 mM TCEP, pH 7.7) to a final salt concentration of ≤100 mM and loaded onto a HiTrap SP HP column (Cytiva). The sample was eluted in a linear gradient of buffer SA2 with 1000 M KCl and then concentrated.

Concentrated $VmFtsN^{1–29}$-ENLYFQ and GG-$VmFtsN^{2–29}$ were further purified by size-exclusion chromatography on a Superdex Peptide 10/300 GL column (Cytiva) equilibrated in NMR buffer (50 mM 2-(N-morpholino)ethanesulfonic acid (MES)–KOH, 50 mM KCl and 1 mM TCEP, pH 6.0). The peak fractions were concentrated to 2–3 mg ml^{-1}, frozen in aliquots and stored at −80 °C. The protein mass was verified by ESI-TOF mass spectrometry.

FtsN peptides. The FtsN peptides were chemically synthesized by Generon/Neobiotech. Purity (≥95% in HPLC) and molecular mass were verified by the company. The lyophilized peptides were resuspended in binding buffer (50 mM HEPES–KOH, 100 mM $(CH_3COO)K$ and 5 mM $(CH_3COO)_2Mg$, pH 7.7). Stock concentrations were determined using an ND-1000 spectrophotometer (NanoDrop Technologies) or a Direct detect infrared spectrometer (Merck Millipore) for peptides without tyrosine and tryptophan residues. The stock concentrations were in the range of 20–70 mM. The peptide sequences are provided in Supplementary Table 5.

Crystal structure determination. The crystallization conditions were screened using our in-house high-throughput crystallization facility[49]. $EcFtsA^{1–405}$ at 7 mg ml^{-1}, $XpFtsA^{1–396}$ at 7 mg ml^{-1} and $VmFtsA^{1–396}$ at 5 mg ml^{-1} were mixed with 2 mM ATP. For co-crystallization, $VmFtsA^{1–396}$ at 3 mg ml^{-1} was mixed with 2 mM ATP and 0.353 mM $VmFtsN^{1–29}$. For $EcFtsA^{1–405}$ and $XpFtsA^{1–396}$, 100 nl protein solution and 100 nl of the crystallization solutions were mixed in MRC sitting-drop crystallization plates for vapour diffusion. To obtain optimized co-crystals of $VmFtsA^{1–396}$ with $VmFtsN^{1–29}$, 500 nl protein solution and 500 nl of the crystallization solutions were used. Optimization for $VmFtsA^{1–396}$ followed the idea of an 'anticipated optimization approach'[50]. The protein solution (250 nl) was mixed with 200 nl of initial crystallization solution (31.55% (vol/vol) PEG 400, 0.21 M $MgCl_2$ and 0.1 M Tris–HCl pH 8.5) and 50 nl of follow-up crystallization solution (10% (vol/vol) 2-propanol, 0.2 M $(CH_3COO)_2Ca$ and 0.1 M MES–NaOH pH 6.0). The plates were incubated at 21 °C. Cryoprotectant solution (1–2 µl) was added to the crystals shortly before mounting single crystals and flash-freezing them in liquid nitrogen. $VmFtsA^{1–396}$–$FtsN^{1–29}$ co-crystals were soaked in cryoprotectant solution for 1 h before mounting. The optimized conditions yielding crystals and cryoprotectant solutions are listed in Supplementary Table 1. Diffraction data were collected on single crystals at Diamond Light Source (Harwell, UK) at 100 K using the in-house Generic Data Acquisition software, as indicated in Supplementary Table 1. The diffraction data were processed using the CCP4 suite[51]. Initial phases were obtained by molecular replacement using PHASER 2.82 and 2.83 (ref. [52]).

The search models are listed in Supplementary Table 1. The models were rebuilt using MAIN 2017 (ref. [53]) and COOT 0.8.9.3 (ref. [54]) and refined using REFMAC 5.8 (ref. [55]) and PHENIX 1.17.1 (ref. [56]). The final statistics are summarized in Supplementary Table 1, and the structure factors as well as atomic coordinates have been deposited in the PDB with the accession codes 7Q6D, 7Q6G, 7Q6F and 7Q6I. Note that the $VmFtsN^{1–29}$ (chains X and Y) density was modelled as $VmFtsN^{1–8}$ for refinement of PDB 7Q6I but deposited as unknown poly-Ala. Structure factors and atomic coordinates for our interpretation of the $VmFtsN^{1–29}$ density (Extended Data Fig. 3d) are provided in Supplementary Data 2.

SPR. Surface plasmon resonance was performed using a Biacore T200 system and CM5-sensor chips (Cytiva). Reference control and analyte channels were equilibrated in binding buffer. FtsA was immobilized onto the chip surface via amide coupling using the supplied kit (Cytiva) to reach a RU value of between 2,000 and 7,800 for separate experiments. The analytes were injected for 120 s, followed by a 300 s dissociation in a 1:2 dilution series with initial concentrations of 10 µM for peptide $EcFtsN^{1–32}$ (Fig. 2b), 60 µM for $VmFtsN^{1–29}$ (Extended Data Fig. 2b) and 20 µM for FtsN peptides (Extended Data Fig. 2i). After reference and buffer signal correction, sensogram data were fitted using Prism 8.0 (GraphPad). The equilibrium response (R_{eq}) data were fitted to a single-site interaction model to determine K_d:

$$R_{eq} = \left(\frac{CR_{max}}{C + K_d}\right) + B, \quad (1)$$

where C is the analyte concentration, R_{max} is the maximum response at saturation and B is the background resonance.

Fluorescence polarization. The peptides $EcFtsN^{1–32}$-C and $VmFtsN^{1–29}$-C were labelled with maleimide-Atto 495 (Merck Life Science). $EcFtsA^{1–405}$ and $VmFtsA^{1–396}$ were buffer exchanged into binding buffer using Zeba spin desalting columns (MWCO of 7 kDa; ThermoFisher) before performing the fluorescence polarization experiments. The labelled peptides (20 nM) were mixed 1:1 with a 1:2 dilution series of protein with initial concentrations of 40 µM for $EcFtsA^{1–405}$ and 120 µM for $VmFtsA^{1–396}$ in binding buffer supplemented with 0.05% (vol/vol) Tween-20 in a 384-well low-flange black flat-bottomed non-binding surface microplate (Corning). The reactions were prepared in triplicate. Fluorescence polarization was measured using a PHERAstar FSX system (BMG Labtech) directly after reaction set-up and after incubation at RT for 30 min and 2 h to ensure equilibrium had been reached. Data were fitted using Prism 8.0 (GraphPad). The dissociation constants were calculated using a two-step model:

$$F = F_0 + \frac{F_{Lo} \times [P_T]}{K_{dLo} + [P_T]} + \frac{F_{Hi} \times [P_T]}{K_{dHi} + [P_T]}, \quad (2)$$

where F_0 is the anisotropy in the absence of titrating protein, $[P_T]$ is the total concentration of protein, and F_{Lo} and F_{Hi} are the anisotropy changes at saturation of low- and high-affinity sites with binding constants of K_{dLo} and K_{dHi}, respectively.

FDS–AUC. The peptides $EcFtsN^{1–32}$-C and $VmFtsN^{1–29}$-C were labelled with maleimide-Atto 495 (Merck Life Science). $EcFtsA^{1–405}$ and $VmFtsA^{1–396}$ were buffer exchanged into binding buffer using Zeba spin desalting columns (MWCO of 7 kDa; ThermoFisher) before the experiments were performed. The labelled peptides (20 nM) were mixed 1:1 with a 1:3 dilution series of protein with initial concentrations of 90 µM for $EcFtsA^{1–405}$ and 120 µM for $VmFtsA^{1–396}$ in binding buffer supplemented with 0.05% (vol/vol) Tween-20. The samples were centrifuged at 163,000*g* and 20 °C in an An50Ti rotor using an Optima XL-I analytical ultracentrifuge (Beckman) equipped with a fluorescence optical system (Aviv Biomedical) with fixed excitation at 488 nm and fluorescence detection at >505 nm. Data were processed and analysed using SEDFIT 16 and SEDPHAT 15.2 (ref. [57]) following the protocol for high-affinity interactions detected by fluorescence[58]. The binding constants were estimated using a two-step model. The data were plotted using GUSSI 1.4.2 (ref. [59]).

Co-pelleting assay. $EcFtsA^{1–405}$ and $VmFtsA^{1–396}$ at 1 mg ml^{-1} (approximately 23 µM) alone or mixed with 0.5-, 1-, 3-, 6- or 10-fold the molar concentration of $EcFtsN^{1–32}$ and $VmFtsN^{1–29}$, respectively, in binding buffer were incubated at 20 °C for 5–15 min before centrifugation at 20,000*g* for 10 min. The supernatant and pellet were carefully separated and analysed by SDS–PAGE. The intensities of the protein bands were quantified using ImageJ 2.1.0 (ref. [60]).

Lipid monolayers and negative-stain electron microscopy. Lipid monolayers were prepared from *E. coli* polar lipid extract (Avanti)[61]. Wells of a custom-made Teflon block were filled with 60 µl binding buffer. Lipids (20 µg), dissolved in chloroform, were applied on top of the buffer and incubated for 2 min. Baked (60 °C, overnight) CF300-Cu-UL electron microscopy grids (EMS) were then placed on top of the wells with the carbon side facing downwards. The grids were incubated for 20–60 min. FtsA, at 0.2 mg ml^{-1} for $EcFtsA^{M96E,R153D}$ and VmFtsA or at 0.1 mg ml^{-1} for all other FtsA variants, was mixed with 1 mM ATP and

the indicated FtsN peptides at a tenfold molar excess, unless stated otherwise, in binding buffer. The samples were incubated for 10 min at RT. The electron microscopy grids were carefully lifted off the buffer and blotted from the side. The samples (4 µl) were applied to the grids and incubated for 30 s before staining with 2% (wt/vol) uranyl formate. The grids were imaged on a Tecnai Spirit electron microscope (ThermoFisher) operating at 120 kV and equipped with a Gatan Orius SC200W camera. The presented micrographs were contrast-adjusted and blurred for display purposes.

Cryo-EM of EcFtsA mini-rings and EcFtsA–FtsN$^{1-32}$ double filaments on lipid monolayers. Lipid monolayers were prepared as described in the 'Lipid monolayers and negative-stain electron microscopy' section, with the exception that Quantifoil Au R0.6/1 300 mesh grids were used. For mini-rings (Extended Data Fig. 3b), EcFtsA at 0.15 mg ml^{-1} was mixed with 1 mM ATP in binding buffer and incubated for 30 min at RT. For double filaments (Fig. 2f), EcFtsA at 0.1 mg ml^{-1} was mixed with 1 mM ATP and EcFtsN$^{1-32}$ at 22 µM in binding buffer and incubated for 20 min at RT. The grids were gently blotted from the side after attachment of the monolayer and inserted into a Vitrobot Mark III (ThermoFisher) set to 20 °C and 100% humidity. The samples (3 µl) were applied to the grid, incubated for 30 s and blotted for 12–15 s (0.5 s drain time; −15 blot force) before plunge-freezing into liquid ethane maintained at −180 °C using a cryostat[62]. For mini-rings, the grids were imaged using a Titan Krios microscope (ThermoFisher) operating at 300 kV and equipped with a Quantum energy filter (Gatan) set to a slit width of 20 eV. Micrographs were collected on a K2-XP direct electron detector at a pixel size of 2.32 Å, −3 to −5 µm defocus and a total dose of 25 e$^-$ Å^{-2} using EPU 2.13 (ThermoFisher). For double filaments, the grids were imaged using a Tecnai G2 Polara microscope (ThermoFisher) operating at 300 kV. Micrographs were collected on a Falcon III direct electron detector at a pixel size of 1.38 Å, −3.3 to −4 µm defocus and a total dose of 100 e$^-$ Å^{-2} using EPU 1.5 (ThermoFisher). Data were processed using MotionCor2 (ref. [63]), CTFFIND4 (ref. [64]) and RELION-3.0 (ref. [65]) for double filaments or RELION-4.0 (ref. [66]) for mini-rings. A total of 162,725 and 104,660 particles were automatically picked and extracted for mini-rings and double filaments, respectively, with the presented 2D class averages corresponding to 14,067 and 14,602 particles, respectively. The presented images were upscaled (Extended Data Fig. 3b), contrast-adjusted and blurred for display purposes.

HDX-MS. VmFtsA$^{1-396}$ at 10 µM was mixed with 2 mM ATP and, if indicated, VmFtsN$^{1-29}$ at a three- or tenfold molar excess in binding buffer. The samples (5 µl) were added to 40 µl of D_2O buffer at RT for 3, 30, 300 and 1,800 s, and then quenched and frozen until further processing. The samples were rapidly thawed and subjected to pepsin cleavage, followed by reversed-phase HPLC separation. The protein was passed through a 2.1 mm × 30 mm, 5 µm Enzymate BEH immobilized pepsin column (Waters) at 200 µl min^{-1} for 2 min. The peptic peptides were trapped and desalted on a 2.1 mm × 5 mm C18 trap column (Acquity BEH C18 Van-guard pre-column, 1.7 µm, Waters). Peptides were eluted over 12 min at 40 µl min^{-1} using a 5–36% gradient of acetonitrile in 0.1% (vol/vol) formic acid. The peptides were separated on a 100 mm × 1 mm, 1.7 µm Acquity UPLC BEH C18 reverse-phase column (Waters). The peptides were detected on a SYNAPT G2-Si HDMS mass spectrometer (Waters) acquiring over a m/z range of 300–2,000, with a standard electrospray ionization source and lock mass calibrated using [Glu1]-fibrino peptide B (50 fmol µl^{-1}). The mass spectrometer was operated at a source temperature of 80 °C and a spray voltage of 2.6 kV. Spectra were collected in positive ion mode. Peptides were identified by MS^e[67] using a 5–36% gradient of acetonitrile in 0.1% (vol/vol) formic acid over 12 min. The resulting mass spectrometry data were analysed using Protein Lynx Global Server 3.0.3 (Waters) with a mass spectrometry tolerance of 5 ppm. Mass analysis of the peptide centroids was performed using DynamX 3.0 (Waters). Only peptides with a score >6.4 were considered. The first round of analysis and identification was performed automatically using DynamX 3.0; however, all peptides (deuterated and non-deuterated) were manually verified at every time point for the correct charge state, presence of overlapping peptides and correct retention time. Deuterium incorporation was not corrected for back-exchange and represents relative, rather than absolute, changes in deuterium levels. Changes in H/D amide exchange in any peptide may be due to a single or multiple amides within that peptide. Time points were prepared in parallel and data for individual time points were acquired on the mass spectrometer on the same day.

NMR. Backbone amide peaks of VmFtsN$^{1-29}$-ENLYFQ were assigned using 167 µM ^{15}N- and ^{13}C-labelled peptide at 278 K in NMR buffer. Standard triple resonance spectra: HNCO, HN(CA)CO, HNCACB and CBCA(CO)NH (Bruker) were collected with 20% non-uniform sampling and processed with compressed sensing using MddNMR 3.2 (ref. [68]). Backbone resonances were assigned using MARS 1.2 (ref. [69]). Topspin 3.6.0 (Bruker) was used for the processing of 2D data and NMRFAM-Sparky 1.47 (ref. [70]) was used for spectra analyses. Assignment of VmFtsN$^{1-29}$-ENLYFQ was transferred and extended to GG-VmFtsN$^{2-29}$ using 295 µM ^{15}N-labelled peptide at 278 K in NMR buffer. The first glycine residue (G0) of GG-VmFtsN$^{2-29}$ was not observed.

For binding studies, ^{1}H, ^{15}N BEST-TROSY spectra were acquired at 278 K on 50 µM GG-VmFtsN$^{2-29}$ mixed with an equimolar concentration of VmFtsA$^{1-396}$ in NMR buffer. As sensitivity was compromised by the formation of FtsA polymers following the binding of FtsN peptide, multiple short experiments were acquired and summed to define the ideal time window for data analysis. Each spectrum was acquired with 128 scans and a recycle delay of 400 ms, with a final spectral resolution of 4.7 Hz per point. The relative peak intensities were normalized to the C-terminal residue R29 of GG-VmFtsN$^{2-29}$ and analysed as I_{bound}/I_{free}, where I_{bound} and I_{free} are the peak intensities of GG-VmFtsN$^{2-29}$ with (bound) and without (free) VmFtsA$^{1-396}$, respectively.

EcFtsA mini-rings and EcFtsA–FtsN$^{1-32}$ filaments on liposomes. Liposomes were prepared from *E. coli* polar lipid extract (Avanti) by extrusion using a mini extruder fitted with a polycarbonate membrane with a pore size of 0.4 µm (Fig. 4b) or 1 µm (Fig. 4a,c; Avanti) in binding buffer (Fig. 4b) or binding buffer without magnesium (Fig. 4a,c) for EcFtsA mini-rings and EcFtsA–EcFtsN$^{1-32}$ filaments, respectively. Pre-formed liposomes at 1 mg ml^{-1} (Fig. 4a,c) or 2 mg ml^{-1} (Fig. 4b) were mixed with 0.5 mM MgATP (Fig. 4a,c) or 1 mM MgATP (Fig. 4b) and proteins at the following concentrations: no proteins (Fig. 4a), FtsA at 20 µM (Fig. 4b), FtsA at 20 µM and FtsN$^{1-32}$ at 200 µM (Fig. 4c, left), and FtsA at 5 µM and FtsN$^{1-32}$ at 50 µM (Fig. 4c, right). The samples were incubated at RT for 30 min without proteins or 10 min with proteins. The samples (3 µl) were applied to a freshly glow-discharged Quantifoil Cu/Rh R2/2 200 (Fig. 4b) or Quantifoil Au R2/2 200 (Fig. 4a,c) mesh grid, blotted for 3.5–7.5 s (0.5 s drain time; −15 blot force) and plunge-frozen into liquid ethane maintained at −180 °C using a cryostat[62] and a Vitrobot Mark III (ThermoFisher) set to 20 °C and 100% humidity. The grids were imaged on a Tecnai F20 microscope (ThermoFisher) equipped with a Falcon II direct electron detector or a Glacios microscope (ThermoFisher) equipped with a Falcon III detector. The microscopes were operated at 200 kV and cryogenic temperature. The presented micrographs were motion-corrected (if collected on Glacios), contrast-adjusted and blurred for display purposes.

EcFtsA–FtsN$^{1-32}$ filaments inside liposomes. EcFtsA–FtsN$^{1-32}$ filaments were encapsulated into liposomes by dilution of CHAPS detergent-solubilized *E. coli* total lipid extract (Avanti)[40]. FtsA (at 20 µM) mixed with 200 µM FtsN$^{1-32}$ and 0.5 mM MgATP in binding buffer without magnesium in a total volume of 50 µl was added to 50 µl of *E. coli* total lipid extract (Avanti) solubilized at 10 mg ml^{-1} in binding buffer without magnesium supplemented with 20 mM CHAPS. The sample was incubated at RT for 35 min before it was gradually diluted (within 20 min) with 500 µl of binding buffer without magnesium supplemented with 0.5 mM MgATP. The samples (3 µl) were applied to a freshly glow-discharged Quantifoil Au R2/2 200 mesh grid, blotted for 5.5–7.5 s (0.5 s drain time; −15 blot force) and plunge-frozen into liquid ethane maintained at −180 °C using a cryostat[62] and a Vitrobot Mark III (ThermoFisher) set to 20 °C and 100% humidity. The grids were imaged on a Tecnai F20 microscope (ThermoFisher) equipped with a Falcon II direct electron detector, operating at 200 kV and cryogenic temperature. Although rare, EcFtsA–FtsN$^{1-32}$ filaments were sometimes observed inside liposomes when added to the outside of pre-formed liposomes (Fig. 4f), most probably due to membrane rearrangements during handling. Here pre-formed liposomes (extruded to 1 µm) at 1 mg ml^{-1} were mixed with 0.5 mM MgATP, FtsA at 2.5 µM and FtsN$^{1-32}$ at 25 µM. The presented micrographs were contrast-adjusted and blurred for display purposes. For 2D class averages (Fig. 4g), micrographs were collected on a Glacios microscope with a Falcon III direct electron detector at a pixel size of 1.99 Å, −2.5 to −4 µm defocus and a total dose of 56 e$^-$ Å^{-2} using SerialEM 3.9 (ref. [71]). Data were processed using MotionCor2 (ref. [63]), CTFFIND4.1 (ref. [64]) and RELION-3.1 (ref. [65]). The presented images were upscaled and blurred for display purposes.

Strain construction. A cloning and recombination strategy based on REXER[72] was used as illustrated in Extended Data Fig. 4a. The helper plasmid pKW20 (NCBI ID: MN927219.1)[72] was used for genome engineering. The acceptor strain SFB123 was created by integrating a *pheS*^{T251A,A294G}–*hygR* double selection cassette downstream of the *lpxC* gene using λ-Red recombineering[73]. *pheS*^{T251A,A294G}/*pheS** confers toxicity through misincorporation of 4-chloro-phenylalanine during translation[74]. We found a long (5 kB) homologous region upstream of FtsA to benefit recombination efficiency. SFB143, an *E. coli* MDS42 *thi*$^-$ strain transformed with the non-transferrable conjugative plasmid pJF146 (NCBI ID: MK809154.1)[75], was used as the donor strain during conjugation. SFB143 cells were made chemically competent[76].

The shuttle plasmid pFB483 was designed with a pMB1 origin of replication, a *pheS*^{T251A,A294G}–*hygR* double selection cassette, a CRISPR array targeting *ftsW* and the region upstream of *secM* and a *ccdB* toxin gene (outsert) flanked by *Bsa*I acceptor sites for Golden Gate assembly[77]. CRISPR arrays were designed to mediate scarless excision. The pFB483 plasmid was propagated in a *ccdB* survival strain.

Targeting constructs were split into 2–3 modules for insertion of single or double point mutations, respectively. Initially, the internal 3×HA tag (120 bp including a *Xho*I restriction site) was inserted into *ftsA* using three modules, resulting in sTN001. Point mutations were introduced by PCR using sTN001 as the template and modules were assembled into pFB483 via Golden Gate assembly with

*Bsa*I. The final targeting construct also introduced a kanamycin-selectable *neoR* marker downstream of the *lpxC* gene. Assembled shuttle vectors were transformed into SFB143 and selected on LB agar plates supplemented with 200 μg ml^{-1} hygromycin B and 50 μg ml^{-1} apramycin at 37 °C.

Acceptor cells (SFB123) were cultured to the stationary phase in 5 ml LB medium supplemented with 10 μg ml^{-1} tetracycline. The culture (4 ml) was harvested by centrifugation and washed three times in LB before being transferred into 50 ml LB supplemented with 10 μg ml^{-1} tetracycline and 0.5% (wt/vol) L-arabinose. The cells were cultured at 37 °C for 1 h, harvested and washed three times in LB. In the meantime, donor transformants were washed off the agar plates using 2 ml LB and left at RT. All cultures were resuspended in LB to an OD_{600} of 40. The acceptor cells (12.5 μl) were mixed with 87.5 μl donor cells and spotted onto well-dried TYE plates. The spots were air-dried before the plates were incubated at 30 °C for 1 h. The cells were washed off the plates with LB and transferred into 50 ml LB supplemented with 12.5 μg ml^{-1} kanamycin and 10 μg ml^{-1} tetracycline. The cells were cultured at 37 °C for 4 h, harvested and plated on LB agar plates supplemented with 12.5 μg ml^{-1} kanamycin, 10 μg ml^{-1} tetracycline, 2% glucose and 2.5 mM 4-chloro-phenylalanine. Strains were single-colony purified and verified by marker analysis and colony PCR, followed by *Xho*I digestion and Sanger sequencing. Strains with the desired point mutations were cured of pKW20 by repeated growth in LB in the absence of antibiotics, diluted 1:10^6 and plated on TYE plates. The strains were verified by marker analysis and Sanger sequencing of PCR products covering the targeting region. The strains used in Fig. 5c were further whole-genome sequenced on a MiSeq (Illumina) system. The next-generation-sequencing data were analysed using breseq v0.35.1 (ref. [78]).

The strains are listed in Supplementary Table 6. Annotated shuttle vectors and genomic loci are provided in Supplementary Data 1 and 3, respectively.

Assessment of growth and cell elongation phenotypes. *Growth on solid media.* Strains were streaked on the same TYE plate and incubated at 37 °C overnight. The next morning, the strains were re-streaked on a fresh TYE plate and incubated at 37 °C for 12 h.

Growth in liquid media. Strains were cultured overnight in LB medium at 37 °C. The cells were diluted 1/1,000 in fresh LB into a 96-well flat-bottomed plate in octuplicate. The plate was incubated at 37 °C in a Tecan microplate reader with regular shaking. Absorbance at a wavelength of 600 nm was measured every 5 min for 24 h. The OD_{600} values were background corrected, normalized to the maximum OD_{600} value of each well and averaged. Individual data points and the means were plotted.

Differential interference contrast imaging of exponential phase cultures. Strains were cultured in LB at 37 °C overnight. The next day, the cells were diluted 1/1,000 in fresh LB and incubated at 37 °C. Cells (2–3 μl) in the exponential phase (OD_{600} = 0.2-0.3) were applied onto an agarose pad and imaged on a Nikon Eclipse E800 microscope equipped with a ×100 oil objective and a Photometrics Iris 9 CMOS camera using a differential interference contrast imaging set-up. The presented images were contrast-adjusted for display purposes.

In vivo cysteine cross-linking. Strains from overnight cultures were cultured in LB medium to the exponential phase (OD_{600} = 0.2–0.4) and 0.9375 OD units were harvested using centrifugation at 4 °C. The cells were kept on ice for the duration of the experiment unless stated otherwise. The cells were washed in 500 μl PBS and resuspended in 50 μl PBS. Dimethylsulfoxide (1.25 μl) or cross-linkers (dBBr, BMOE, BMB or BMH) in dimethylsulfoxide (20 mM stock) were added to the cells. The samples were incubated for 10 min and quenched by adding 1 μl 2-ME (1.43 M stock in Millipore water). The cells were resuspended in 50 μl lysis buffer (1 mM EDTA (pH 7.4), 14.3 mM 2-ME, cOmplete EDTA-free protease inhibitor cocktail (Roche), 0.25 U μl^{-1} benzonase (Merck) and 0.5 U μl^{-1} ReadyLyse lysozyme (Lucigen) in B-PER (ThermoFisher)). The samples were incubated at RT for 5 min and 50 μl of 2×SDS sample loading buffer supplemented with 3% (vol/vol) 2-ME was added. The samples were incubated at 95 °C for 5 min and the equivalent of 0.1875 OD units of cells was analysed by SDS–PAGE. Western blotting was performed using a Trans-Blot turbo system (Bio-Rad) with the corresponding Midi 0.2 μm PVDF transfer pack. The blots were run at 25 V and 2.5 A for 7 min. The membranes were blocked in PBS + 5% milk for 30–40 min, washed in PBS and incubated with anti-HA-peroxidase (Roche, 12013819001; 1/1,000 in PBST + 5% milk) at RT for 1–1.5 h. The membranes were then thoroughly washed with PBST, developed using an ECL prime western blotting detection kit (Amersham/Cytiva) and imaged on a Gel DocTM XR+ system (Bio-Rad). The presented images were contrast-adjusted for display purposes.

Reporting summary. Further information on research design is available in the Nature Research Reporting Summary linked to this article.

Data availability

Atomic coordinates have been deposited in the PDB with accession codes 7Q6D (*E. coli* FtsA$^{1–405}$), 7Q6G (*X. poinarii* FtsA$^{1–396}$), 7Q6F (*V. maritimus* FtsA$^{1–396}$, antiparallel double filament) and 7Q6I (*V. maritimus* FtsA$^{1–396}$ and FtsN$^{1–29}$, bent tetramers in antiparallel double filament arrangement). The next-generation sequencing data associated with this study are available from the Sequence Read Archive at BioProject PRJNA852398. PDB entries 1E4F, 1E4G, 2YCH, 3WQT, 3WQU, 3WT0, 4A2A, 4A2B and 4CZJ were used for structural superpositions and analyses. Source data are provided with this paper.

Received: 17 December 2021; Accepted: 19 July 2022;
Published online: 19 September 2022

References

1. Typas, A., Banzhaf, M., Gross, C. A. & Vollmer, W. From the regulation of peptidoglycan synthesis to bacterial growth and morphology. *Nat. Rev. Microbiol.* **10**, 123–136 (2011).
2. Szwedziak, P. & Löwe, J. Do the divisome and elongasome share a common evolutionary past. *Curr. Opin. Microbiol.* **16**, 745–751 (2013).
3. Pichoff, S. & Lutkenhaus, J. Tethering the Z ring to the membrane through a conserved membrane targeting sequence in FtsA. *Mol. Microbiol.* **55**, 1722–1734 (2005).
4. Salje, J., van den Ent, F., de Boer, P. & Löwe, J. Direct membrane binding by bacterial actin MreB. *Mol. Cell* **43**, 478–487 (2011).
5. Pichoff, S. & Lutkenhaus, J. Unique and overlapping roles for ZipA and FtsA in septal ring assembly in *Escherichia coli*. *EMBO J.* **21**, 685–693 (2002).
6. Nogales, E., Downing, K. H., Amos, L. A. & Löwe, J. Tubulin and FtsZ form a distinct family of GTPases. *Nat. Struct. Biol.* **5**, 451–458 (1998).
7. Bisson-Filho, A. W. et al. Treadmilling by FtsZ filaments drives peptidoglycan synthesis and bacterial cell division. *Science* **355**, 739–743 (2017).
8. Yang, X. et al. GTPase activity-coupled treadmilling of the bacterial tubulin FtsZ organizes septal cell wall synthesis. *Science* **355**, 744–747 (2017).
9. Monteiro, J. M. et al. Peptidoglycan synthesis drives an FtsZ-treadmilling-independent step of cytokinesis. *Nature* **554**, 528–532 (2018).
10. Squyres, G. R. et al. Single-molecule imaging reveals that Z-ring condensation is essential for cell division in *Bacillus subtilis*. *Nat. Microbiol.* **6**, 553–562 (2021).
11. Whitley, K. D. et al. FtsZ treadmilling is essential for Z-ring condensation and septal constriction initiation in *Bacillus subtilis* cell division. *Nat. Commun.* **12**, 2448 (2021).
12. Karimova, G., Dautin, N. & Ladant, D. Interaction network among *Escherichia coli* membrane proteins involved in cell division as revealed by bacterial two-hybrid analysis. *J. Bacteriol.* **187**, 2233–2243 (2005).
13. Du, S. & Lutkenhaus, J. Assembly and activation of the *Escherichia coli* divisome. *Mol. Microbiol.* **105**, 177–187 (2017).
14. Pichoff, S., Du, S. & Lutkenhaus, J. Disruption of divisome assembly rescued by FtsN–FtsA interaction in *Escherichia coli*. *Proc. Natl Acad. Sci. USA* https://doi.org/10.1073/pnas.1806450115 (2018).
15. Gerding, M. A. et al. Self-enhanced accumulation of FtsN at division sites and roles for other proteins with a SPOR domain (DamX, DedD, and RlpA) in *Escherichia coli* cell constriction. *J. Bacteriol.* **191**, 7383–7401 (2009).
16. Liu, B., Persons, L., Lee, L. & de Boer, P. A. Roles for both FtsA and the FtsBLQ subcomplex in FtsN-stimulated cell constriction in *Escherichia coli*. *Mol. Microbiol.* **95**, 945–970 (2015).
17. Tsang, M. J. & Bernhardt, T. G. A role for the FtsQLB complex in cytokinetic ring activation revealed by an *ftsL* allele that accelerates division. *Mol. Microbiol.* **95**, 925–944 (2015).
18. Marmont, L. S. & Bernhardt, T. G. A conserved subcomplex within the bacterial cytokinetic ring activates cell wall synthesis by the FtsW–FtsI synthase. *Proc. Natl Acad. Sci. USA* **117**, 23879–23885 (2020).
19. Li, Y. et al. Genetic analysis of the septal peptidoglycan synthase FtsWI complex supports a conserved activation mechanism for SEDS–bPBP complexes. *PLoS Genet.* **17**, e1009366 (2021).
20. Busiek, K. K. & Margolin, W. A role for FtsA in SPOR-independent localization of the essential *Escherichia coli* cell division protein FtsN. *Mol. Microbiol.* **92**, 1212–1226 (2014).
21. van den Ent, F. & Löwe, J. Crystal structure of the cell division protein FtsA from *Thermotoga maritima*. *EMBO J.* **19**, 5300–5307 (2000).
22. Busiek, K. K., Eraso, J. M., Wang, Y. & Margolin, W. The early divisome protein FtsA interacts directly through its 1c subdomain with the cytoplasmic domain of the late divisome protein FtsN. *J. Bacteriol.* **194**, 1989–2000 (2012).
23. Pichoff, S., Du, S. & Lutkenhaus, J. The bypass of ZipA by overexpression of FtsN requires a previously unknown conserved FtsN motif essential for FtsA–FtsN interaction supporting a model in which FtsA monomers recruit late cell division proteins to the Z ring. *Mol. Microbiol.* **95**, 971–987 (2015).
24. Baranova, N. et al. Diffusion and capture permits dynamic coupling between treadmilling FtsZ filaments and cell division proteins. *Nat. Microbiol.* https://doi.org/10.1038/s41564-019-0657-5 (2020).
25. Corbin, B. D., Geissler, B., Sadasivam, M. & Margolin, W. Z-ring-independent interaction between a subdomain of FtsA and late septation proteins as revealed by a polar recruitment assay. *J. Bacteriol.* **186**, 7736–7744 (2004).

26. Rico, A. I., Garcia-Ovalle, M., Mingorance, J. & Vicente, M. Role of two essential domains of *Escherichia coli* FtsA in localization and progression of the division ring. *Mol. Microbiol.* **53**, 1359–1371 (2004).
27. Bernard, C. S., Sadasivam, M., Shiomi, D. & Margolin, W. An altered FtsA can compensate for the loss of essential cell division protein FtsN in *Escherichia coli*. *Mol. Microbiol.* **64**, 1289–1305 (2007).
28. Pichoff, S., Shen, B., Sullivan, B. & Lutkenhaus, J. FtsA mutants impaired for self-interaction bypass ZipA suggesting a model in which FtsA's self-interaction competes with its ability to recruit downstream division proteins. *Mol. Microbiol.* **83**, 151–167 (2012).
29. Radler, P. et al. In vitro reconstitution of *Escherichia coli* divisome activation. *Nat. Commun.* **13**, 2635 (2022).
30. Szwedziak, P., Wang, Q., Freund, S. M. & Löwe, J. FtsA forms actin-like protofilaments. *EMBO J.* **31**, 2249–2260 (2012).
31. Wagstaff, J. & Löwe, J. Prokaryotic cytoskeletons: protein filaments organizing small cells. *Nat. Rev. Microbiol.* **16**, 187–201 (2018).
32. Schoenemann, K. M. et al. Gain-of-function variants of FtsA form diverse oligomeric structures on lipids and enhance FtsZ protofilament bundling. *Mol. Microbiol.* https://doi.org/10.1111/mmi.14069 (2018).
33. van den Ent, F., Izore, T., Bharat, T. A., Johnson, C. M. & Löwe, J. Bacterial actin MreB forms antiparallel double filaments. *eLife* **3**, e02634 (2014).
34. Hussain, S. et al. MreB filaments align along greatest principal membrane curvature to orient cell wall synthesis. *eLife* https://doi.org/10.7554/eLife.32471 (2018).
35. Wong, F., Garner, E. C. & Amir, A. Mechanics and dynamics of translocating MreB filaments on curved membranes. *eLife* https://doi.org/10.7554/eLife.40472 (2019).
36. Dion, M. F. et al. *Bacillus subtilis* cell diameter is determined by the opposing actions of two distinct cell wall synthetic systems. *Nat. Microbiol.* **4**, 1294–1305 (2019).
37. Krupka, M. et al. *Escherichia coli* FtsA forms lipid-bound minirings that antagonize lateral interactions between FtsZ protofilaments. *Nat. Commun.* **8**, 15957 (2017).
38. Hayward, S. & Lee, R. A. Improvements in the analysis of domain motions in proteins from conformational change: DynDom version 1.50. *J. Mol. Graph. Model.* **21**, 181–183 (2002).
39. Karuppiah, V. & Derrick, J. P. Structure of the PilM–PilN inner membrane type IV pilus biogenesis complex from *Thermus thermophilus*. *J. Biol. Chem.* **286**, 24434–24442 (2011).
40. Szwedziak, P., Wang, Q., Bharat, T. A., Tsim, M. & Löwe, J. Architecture of the ring formed by the tubulin homologue FtsZ in bacterial cell division. *eLife* **3**, e04601 (2014).
41. Bendezu, F. O., Hale, C. A., Bernhardt, T. G. & de Boer, P. A. RodZ (YfgA) is required for proper assembly of the MreB actin cytoskeleton and cell shape in *E. coli*. *EMBO J.* **28**, 193–204 (2009).
42. McQuillen, R. & Xiao, J. Insights into the structure, function, and dynamics of the bacterial cytokinetic FtsZ-ring. *Annu. Rev. Biophys.* https://doi.org/10.1146/annurev-biophys-121219-081703 (2020).
43. Du, S. & Lutkenhaus, J. At the heart of bacterial cytokinesis: the Z ring. *Trends Microbiol.* **27**, 781–791 (2019).
44. Park, K. T., Pichoff, S., Du, S. & Lutkenhaus, J. FtsA acts through FtsW to promote cell wall synthesis during cell division in *Escherichia coli*. *Proc. Natl Acad. Sci. USA* https://doi.org/10.1073/pnas.2107210118 (2021).
45. Taguchi, A. et al. FtsW is a peptidoglycan polymerase that is functional only in complex with its cognate penicillin-binding protein. *Nat. Microbiol.* **4**, 587–594 (2019).
46. Cho, H. et al. Bacterial cell wall biogenesis is mediated by SEDS and PBP polymerase families functioning semi-autonomously. *Nat. Microbiol.* **1**, 16172 (2016).
47. Sjodt, M. et al. Structural coordination of polymerization and crosslinking by a SEDS–bPBP peptidoglycan synthase complex. *Nat. Microbiol.* htttps://doi.org/10.1038/s41564-020-0687-z (2020).
48. Jacquier, N., Viollier, P. H. & Greub, G. The role of peptidoglycan in chlamydial cell division: towards resolving the chlamydial anomaly. *FEMS Microbiol. Rev.* **39**, 262–275 (2015).
49. Gorrec, F. & Löwe, J. Automated protocols for macromolecular crystallization at the MRC laboratory of molecular biology. *J. Vis. Exp.* https://doi.org/10.3791/55790 (2018).
50. Gorrec, F. An anticipated optimization approach to macromolecular crystallization. Preprint at *bioRxiv* https://doi.org/10.1101/620328 (2019).
51. Winn, M. D. et al. Overview of the CCP4 suite and current developments. *Acta Crystallogr. D* **67**, 235–242 (2011).
52. McCoy, A. J. et al. Phaser crystallographic software. *J. Appl. Crystallogr.* **40**, 658–674 (2007).
53. Turk, D. MAIN software for density averaging, model building, structure refinement and validation. *Acta Crystallogr. D* **69**, 1342–1357 (2013).
54. Emsley, P., Lohkamp, B., Scott, W. G. & Cowtan, K. Features and development of Coot. *Acta Crystallogr. D* **66**, 486–501 (2010).
55. Murshudov, G. N., Vagin, A. A. & Dodson, E. J. Refinement of macromolecular structures by the maximum-likelihood method. *Acta Crystallogr. D* **53**, 240–255 (1997).
56. Afonine, P. V. et al. Real-space refinement in PHENIX for cryo-EM and crystallography. *Acta Crystallogr. D* **74**, 531–544 (2018).
57. Schuck, P. On the analysis of protein self-association by sedimentation velocity analytical ultracentrifugation. *Anal. Biochem.* **320**, 104–124 (2003).
58. Chaturvedi, S. K., Ma, J., Zhao, H. & Schuck, P. Use of fluorescence-detected sedimentation velocity to study high-affinity protein interactions. *Nat. Protoc.* **12**, 1777–1791 (2017).
59. Brautigam, C. A. Calculations and publication-quality illustrations for analytical ultracentrifugation data. *Methods Enzymol.* **562**, 109–133 (2015).
60. Abràmoff, M. D., Magalhães, P. J. & Ram, S. J. Image processing with ImageJ. *Biophotonics Int.* **11**, 36–42 (2004).
61. Levy, D. et al. Two-dimensional crystallization on lipid layer: a successful approach for membrane proteins. *J. Struct. Biol.* **127**, 44–52 (1999).
62. Russo, C. J., Scotcher, S. & Kyte, M. A precision cryostat design for manual and semi-automated cryo-plunge instruments. *Rev. Sci. Instrum.* **87**, 114302 (2016).
63. Zheng, S. Q. et al. MotionCor2: anisotropic correction of beam-induced motion for improved cryo-electron microscopy. *Nat. Methods* **14**, 331–332 (2017).
64. Rohou, A. & Grigorieff, N. CTFFIND4: fast and accurate defocus estimation from electron micrographs. *J. Struct. Biol.* **192**, 216–221 (2015).
65. Zivanov, J. et al. New tools for automated high-resolution cryo-EM structure determination in RELION-3. *eLife* https://doi.org/10.7554/eLife.42166 (2018).
66. Kimanius, D., Dong, L., Sharov, G., Nakane, T. & Scheres, S. H. W. New tools for automated cryo-EM single-particle analysis in RELION-4.0. *Biochem. J.* **478**, 4169–4185 (2021).
67. Silva, J. C. et al. Quantitative proteomic analysis by accurate mass retention time pairs. *Anal. Chem.* **77**, 2187–2200 (2005).
68. Jaravine, V. A., Zhuravleva, A. V., Permi, P., Ibraghimov, I. & Orekhov, V. Y. Hyperdimensional NMR spectroscopy with nonlinear sampling. *J. Am. Chem. Soc.* **130**, 3927–3936 (2008).
69. Jung, Y. S. & Zweckstetter, M. Mars—robust automatic backbone assignment of proteins. *J. Biomol. NMR* **30**, 11–23 (2004).
70. Lee, W., Tonelli, M. & Markley, J. L. NMRFAM-SPARKY: enhanced software for biomolecular NMR spectroscopy. *Bioinformatics* **31**, 1325–1327 (2015).
71. Mastronarde, D. N. Automated electron microscope tomography using robust prediction of specimen movements. *J. Struct. Biol.* **152**, 36–51 (2005).
72. Wang, K. et al. Defining synonymous codon compression schemes by genome recoding. *Nature* **539**, 59–64 (2016).
73. Yu, D. et al. An efficient recombination system for chromosome engineering in *Escherichia coli*. *Proc. Natl Acad. Sci. USA* **97**, 5978–5983 (2000).
74. Miyazaki, K. Molecular engineering of a PheS counterselection marker for improved operating efficiency in *Escherichia coli*. *Biotechniques* **58**, 86–88 (2015).
75. Fredens, J. et al. Total synthesis of *Escherichia coli* with a recoded genome. *Nature* **569**, 514–518 (2019).
76. Inoue, H., Nojima, H. & Okayama, H. High efficiency transformation of *Escherichia coli* with plasmids. *Gene* **96**, 23–28 (1990).
77. Engler, C., Kandzia, R. & Marillonnet, S. A one pot, one step, precision cloning method with high throughput capability. *PLoS ONE* **3**, e3647 (2008).
78. Deatherage, D. E. & Barrick, J. E. Identification of mutations in laboratory-evolved microbes from next-generation sequencing data using breseq. *Methods Mol. Biol.* **1151**, 165–188 (2014).

Acknowledgements

We thank D. Bellini, F. Gorrec and M. Yu (MRC LMB) for many helpful discussions on crystallization and help with synchrotron data collection; the staff at Diamond Light Source beamlines I03 and I04 for excellent technical support; G. Cannone, C. Savva and all of the members of the LMB electron microscopy facility for training and support; G. Cannone and Y. Liu for help with electron microscopy data collection; T. Darling and J. Grimmett for help with computing infrastructure; K. Liu for next-generation-sequencing library preparation; and all members of the Löwe group for discussions and technical help (all MRC LMB). T.N. was supported by a Boehringer Ingelheim Fonds PhD fellowship and a Vice-Chancellor's Award by the Cambridge Commonwealth, European and International Trust. F.B. was supported by an EMBO Advanced fellowship (grant no. ALTF 605-2019). This work was funded by the Medical Research Council (grant nos U105181009 and UPA0241008 to J.W.C, and U105184326 to J.L.) and Wellcome (grant no. 202754/Z/16/Z to J.L.).

Author contributions

T.N. performed protein purifications, electron microscopy, co-pelleting, in vivo cysteine cross-linking and strain characterization. S.H.M. performed the SPR, fluorescence polarization and FDS–AUC experiments. T.N., D.K.-C. and J.L. performed crystallization and crystallography. S.L.M. and J.M.S. performed the HDX-MS experiments. C.W.H.Y.

and S.M.V.F. performed the NMR experiments and assignments. L.F.H.F. designed the genome mutagenesis strategy under the supervision of J.W.C., which was adapted by F.B. for combinatorial mutagenesis. T.N. and F.B. performed genome engineering. T.N. and L.F.H.F. performed next-generation sequencing. J.L. supervised the study. T.N. and J.L. wrote the manuscript, with contributions from all authors.

Competing interests

The authors declare no competing interests.

Additional information

Extended data is available for this paper at https://doi.org/10.1038/s41564-022-01206-9.

Supplementary information The online version contains supplementary material available at https://doi.org/10.1038/s41564-022-01206-9.

Correspondence and requests for materials should be addressed to Jan Löwe.

Peer review information *Nature Microbiology* thanks Rut Carballido-Lopez, William Margolin and Felipe Merino for their contribution to the peer review of this work. Peer reviewer reports are available.

Reprints and permissions information is available at www.nature.com/reprints.

Publisher's note Springer Nature remains neutral with regard to jurisdictional claims in published maps and institutional affiliations.

Springer Nature or its licensor holds exclusive rights to this article under a publishing agreement with the author(s) or other rightsholder(s); author self-archiving of the accepted manuscript version of this article is solely governed by the terms of such publishing agreement and applicable law.

© The Author(s), under exclusive licence to Springer Nature Limited 2022

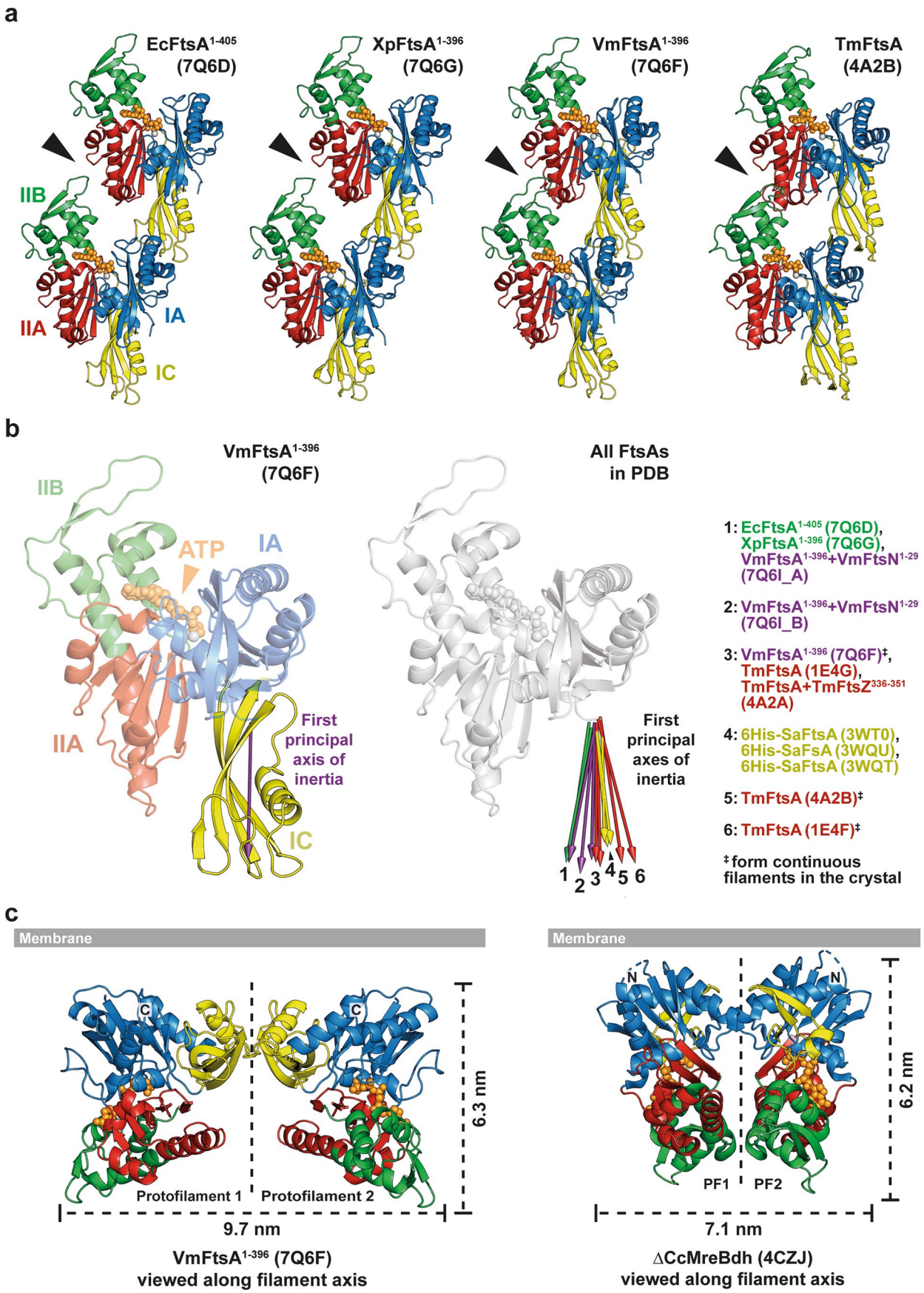

Extended Data Fig. 1 | See next page for caption.

Extended Data Fig. 1 | The position of the IC domain within the FtsA monomer varies. a, Comparison of longitudinal filament contacts in FtsA crystal structures from *E. coli* (PDB 7Q6D), *X. poinarii* (PDB 7Q6G), *V. maritimus* (PDB 7Q6F) and *T. maritima* (PDB 4A2B). *E. coli* and *X. poinarii* FtsA form 'loose' protofilaments with detached IIA and IIB domains (arrowhead). IIA and IIB domains are in close contact in the VmFtsA and TmFtsA structures, which form continuous filaments in the crystals. **b**, The IC domain of FtsA is flexible. Left: an arrow along the first principal axis of inertia of the IC domain (purple) can be used to indicate IC domain orientation. Right: FtsA structures in the PDB aligned on their IA, IIA and IIB domains, with arrows indicating the position of the IC domains, showing that the IC domain orientation is variable within the FtsA monomer. There is no correlation between IC domain position and species (different colours) or formation of continuous filaments in the crystals (³). Principal axes of inertia were calculated using main chain atoms (N, CA, C) of IC domains. **c**, Comparison between the FtsA and MreB double filaments. Because the lateral interface is formed by the IC domain in the FtsA double filament, it is wider than the MreB double filament. The membrane-proximal side of both double filaments is flat.

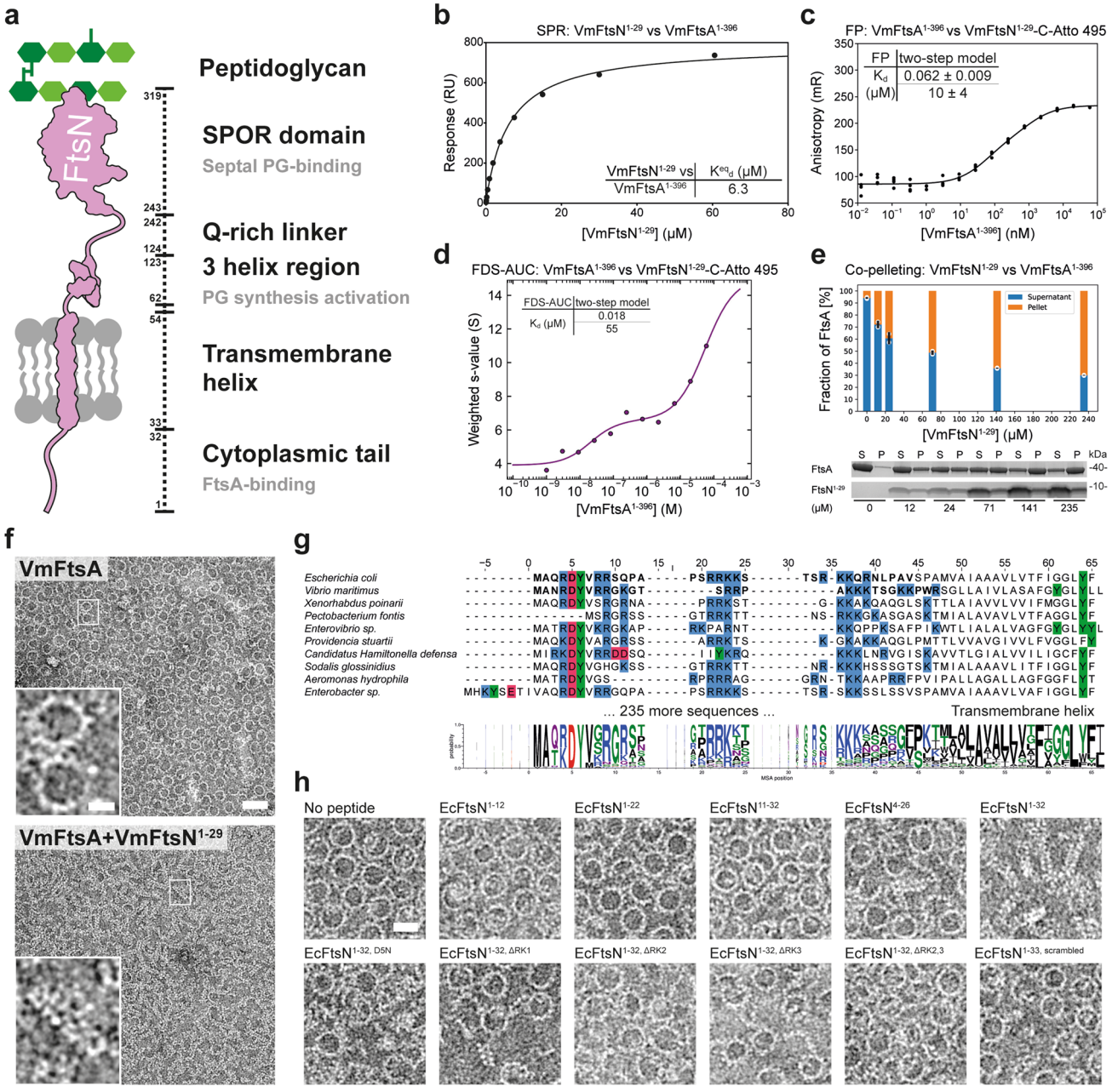

i

Peptide	Sequence	SPR K^{eq}_d (μM)	EM
EcFtsN$^{1-12}$	MAQRD YVRRS QP	ND	Rings
EcFtsN$^{1-22}$	MAQRD YVRRS QPAPS RRKKS TS	93.5 ± 41.5*	Rings
EcFtsN$^{11-32}$	QPAPS RRKKS TSRKK QRNLP AV	8.6 ± 0.8	Rings
EcFtsN$^{4-26}$	RD YVRRS QPAPS RRKKS TSRKK Q	3.8 ± 0.4	Rings
EcFtsN$^{1-32}$	MAQRD YVRRS QPAPS RRKKS TSRKK QRNLP AV	1.6 ± 0.1	Doublets
EcFtsN$^{1-32,\ D5N}$	MAQR**N** YVRRS QPAPS RRKKS TSRKK QRNLP AV	0.85 ± 0.25	Undefined
EcFtsN$^{1-32,\ \Delta RK1}$	MAQRD YV**AA**S QPAPS RRKKS TSRKK QRNLP AV	11.6 ± 0.8	Rings
EcFtsN$^{1-32,\ \Delta RK2}$	MAQRD YVRRS QPAPS **AASA**S TSRKK QRNLP AV	166 ± 34*	Rings
EcFtsN$^{1-32,\ \Delta RK3}$	MAQRD YVRRS QPAPS RRKKS TS**ASA** QRNLP AV	80.6 ± 36*	Rings
EcFtsN$^{1-32,\ \Delta RK2,3}$	MAQRD YVRRS QPAPS **AASA**S TS**ASA** QRNLP AV	ND	Rings
EcFtsN$^{1-33,\ scrambled}$	SARRK NKRRV RQVRK TAPPQ QDSSP LKAMS RYS	1.6 ± 0.4	Rings

Extended Data Fig. 2 | See next page for caption.

Extended Data Fig. 2 | VmFtsA forms antiparallel double filaments upon binding VmFtsN$^{1-29}$. a, Schematic overview of EcFtsN. **b**, SPR equilibrium response titration of VmFtsN$^{1-29}$ binding to immobilized VmFtsA$^{1-396}$. Binding affinity is about threefold lower than for the EcFtsA$^{1-405}$-EcFtsN$^{1-32}$ interaction (Fig. 2b). **c**, VmFtsA$^{1-396}$ titration into VmFtsN$^{1-29}$-C-Atto 495. Data were fitted with a two-step model, with transitions being indicative of FtsN binding and polymerization (**d**). A representative quadruplicate is shown. Kds are given as mean ± SEM from five independent experiments. **d**, Weight-averaged sedimentation coefficients of a VmFtsA$^{1-396}$ titration into VmFtsN$^{1-29}$-C-Atto 495 by FDS–AUC show that VmFtsN$^{1-29}$ is part of higher order FtsA polymers. Data were fitted to a two-step model, recapitulating the FP data in **c**. **e**, Co-pelleting assay of VmFtsN$^{1-29}$ titrated into VmFtsA$^{1-396}$ indicates that VmFtsN$^{1-29}$ induces FtsA polymerization. A representative SDS–PAGE gel is shown. Given are mean ± sd (black lines) of technical duplicates (white dots). P: pellet, S: supernatant. **f**, Negative-stain electron micrographs of VmFtsA with and without VmFtsN$^{1-29}$ on supported lipid monolayers. VmFtsA forms 'mini-rings' in the absence of FtsN and double filaments at tenfold molar excess of VmFtsN$^{1-29}$. Two independent grids were examined per condition. Scale bar, 50 nm, 20 nm (inset). **g**, Multiple sequence alignment of 245 FtsN sequences comprising cytoplasmic and transmembrane domains. EcFtsN$^{1-32}$ and VmFtsN$^{1-29}$ sequences are highlighted in bold. **h**, Mapping of the FtsA-interacting region in EcFtsN$^{1-32}$ using the lipid monolayer assay. EcFtsN$^{1-32}$ mutants were in tenfold molar excess of FtsA. In contrast to EcFtsN$^{1-32}$, EcFtsN$^{1-32, D5N}$ and a scrambled version of the EcFtsN$^{1-32}$ peptide[24] did not induce FtsA double filaments. EcFtsN$^{4-26}$ and EcFtsN$^{1-32, \Delta RK1}$ led to formation of fewer double filaments. At least two independent grids were examined per condition. Scale bar, 20 nm. **i**, Summary of EcFtsN$^{1-32}$ peptides. Mutations are highlighted in bold. Equilibrium dissociation constants (K^{eq}_{d}) are given as mean ± SEM ($n \geq 2$ for each construct). For weak binders the maximum response was fixed during fitting, hence these are only approximate values as indicated by asterisks. ND: not determinable. The predominant higher order polymer observed in the monolayer assay is given in the 'EM' column. Note that EcFtsN$^{4-26}$ and EcFtsN$^{1-32, \Delta RK1}$ still lead to formation of a few FtsA double filaments.

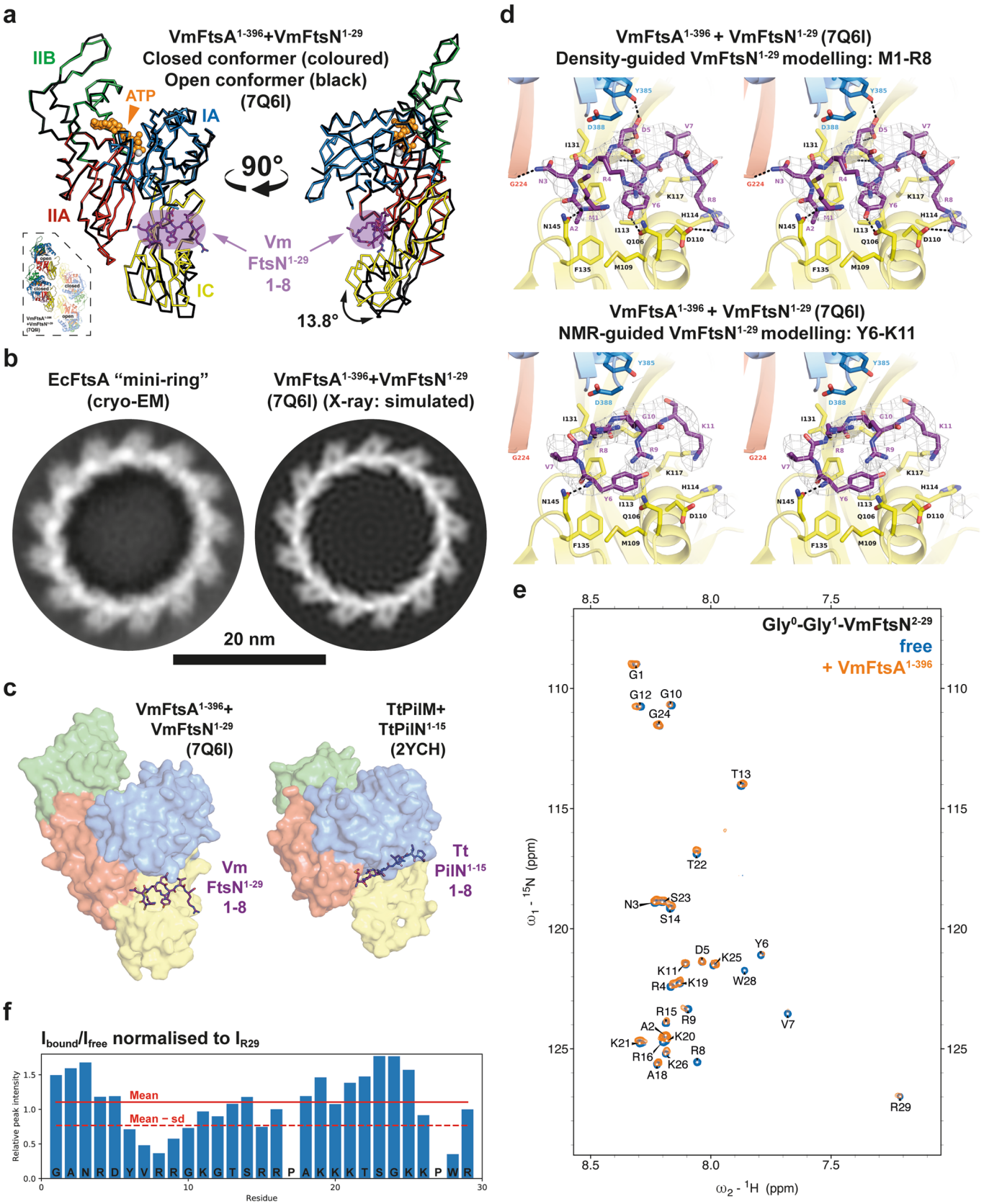

Extended Data Fig. 3 | See next page for caption.

Extended Data Fig. 3 | Modelling of VmFtsN$^{1-29}$ binding to VmFtsA$^{1-396}$. a, Comparison between the peptide-bound closed (coloured) and peptide-free open conformer (black) of FtsA in the VmFtsA$^{1-396}$-VmFtsN$^{1-29}$ co-crystal structure (PDB 7Q6I). The IC domain of the open conformer is rotated 13.8° downwards compared to the closed conformer, as determined by analysis with DynDom[38]. Consequently, the open conformation is likely incompatible with VmFtsN$^{1-29}$ binding. The inset shows the position of open and closed conformers within the tetramer. **b**, Left: EcFtsA forms 'mini-rings' on lipid monolayers as determined by cryo-EM. Two independent grids were examined. Data was collected on one grid. Right: a computed 2D projection after expansion of a longitudinal dimer from the VmFtsA$^{1-396}$-VmFtsN$^{1-29}$ co-crystal structure (PDB 7Q6I) is shown for comparison. The expanded longitudinal dimer does not form a closed ring but a helix. The comparison illustrates that FtsA's IA domains are facing outwards. Scale bar, 20 nm. **c**, Comparison between the *V. maritimus* FtsA–FtsN and *Thermus thermophilus* PilM-PilN (PDB 2YCH) interaction sites[39]. Both binding sites are in the IA–IC interdomain cleft of FtsA and PilM but occupy distinct subspaces. FtsN predominantly contacts the IC domain of FtsA, whereas PilN binds closer to the IA domain of PilM. **d**, Stereo images of the FtsA–FtsN interaction site in the VmFtsA$^{1-396}$-VmFtsN$^{1-29}$ co-crystal structure (PDB 7Q6I). Top: our preferred interpretation of the electron density corresponding to VmFtsN$^{1-29}$, with residues M1-R8 modelled (purple). Side chains of FtsA residues in the interaction site are shown as sticks and polar contacts are marked with black, dashed lines. Bottom: electron density interpretation guided by the NMR data instead (**e** and **f**), with residues Y6-K11 of VmFtsN$^{1-29}$ modelled (purple). Electron density maps (grey) are shown at 1.2 sigma. **e**, ^{1}H, ^{15}N 2D-HSQC NMR spectrum of free GG-VmFtsN$^{2-29}$ (blue) and with equimolar amounts of FtsA added (orange). To follow VmFtsN numbering, the first glycine of GG-VmFtsN$^{2-29}$ is assigned as G0. **f**, Changes in relative peak intensity expressed as I_{bound}/I_{free} with intensities normalized to I_{R29}, which is assumed not to be involved in the VmFtsA-FtsN interaction.

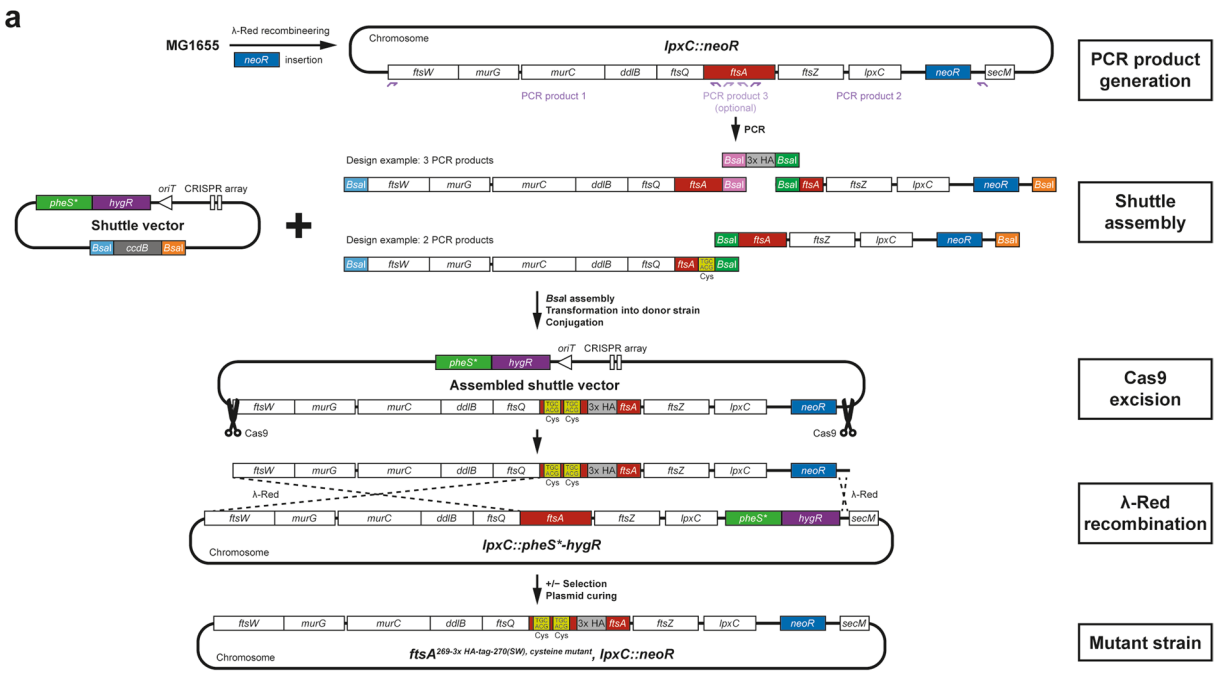

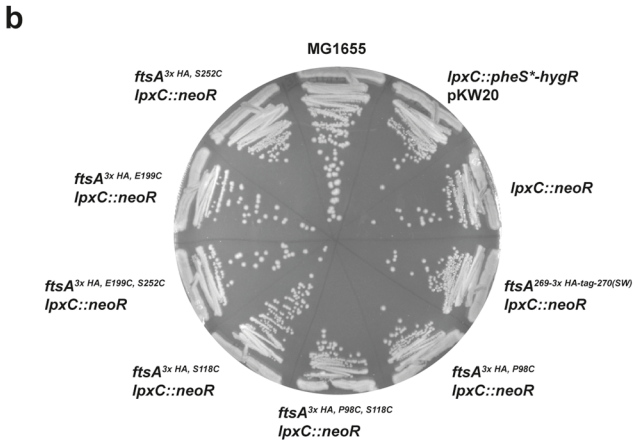

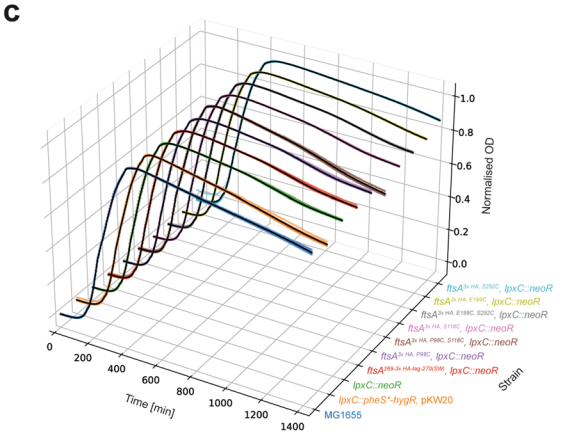

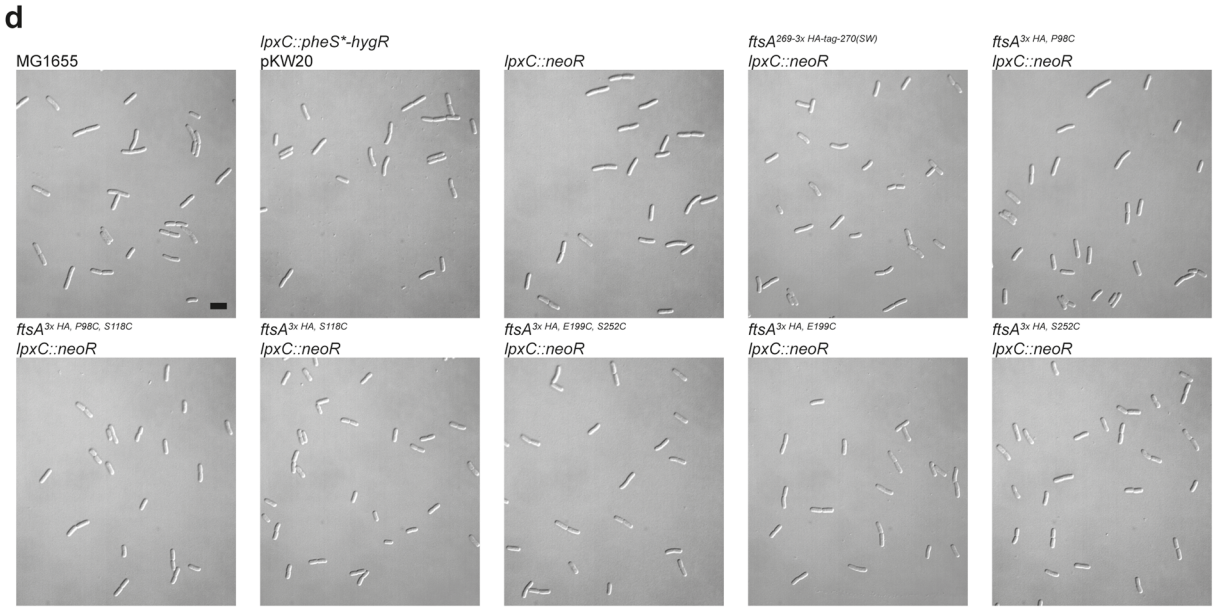

Extended Data Fig. 4 | See next page for caption.

Extended Data Fig. 4 | FtsA cysteine mutant strains: generation and absence of phenotype changes. a, Workflow for REXER[72]-based strain construction. PCR products containing the 3×HA tag or cysteine point mutations were inserted into a shuttle vector by Golden Gate assembly[77]. Assembled shuttle vectors were transformed into the donor strain, conjugated, and excised *in vivo* using Cas9. Targeting constructs contain homology regions for λ-Red mediated recombination into the target locus. Recombinants were selected for *neoR* and *tetR* markers and against the *pheS** marker. Strains were cured of the helper plasmid pKW20 by growth in the absence of selection. **b**, Growth of strains containing single or double cysteine point mutations and a 3×HA tag in the endogenous *ftsA* gene, and a kanamycin resistance cassette inserted after the *lpxC* gene. Parent strains and the original MG1655 strain are also shown. SW: sandwich fusion. **c**, Growth curves of the same strains in liquid LB medium. Plotted are traces of technical octuplicates (coloured) with mean (black). **d**, DIC images of the same strains in the exponential phase (OD_{600} = 0.2-0.3) demonstrating the absence of elongated cells. Similar results were achieved in biological triplicate, of which one was imaged using DIC and two were imaged using phase contrast.

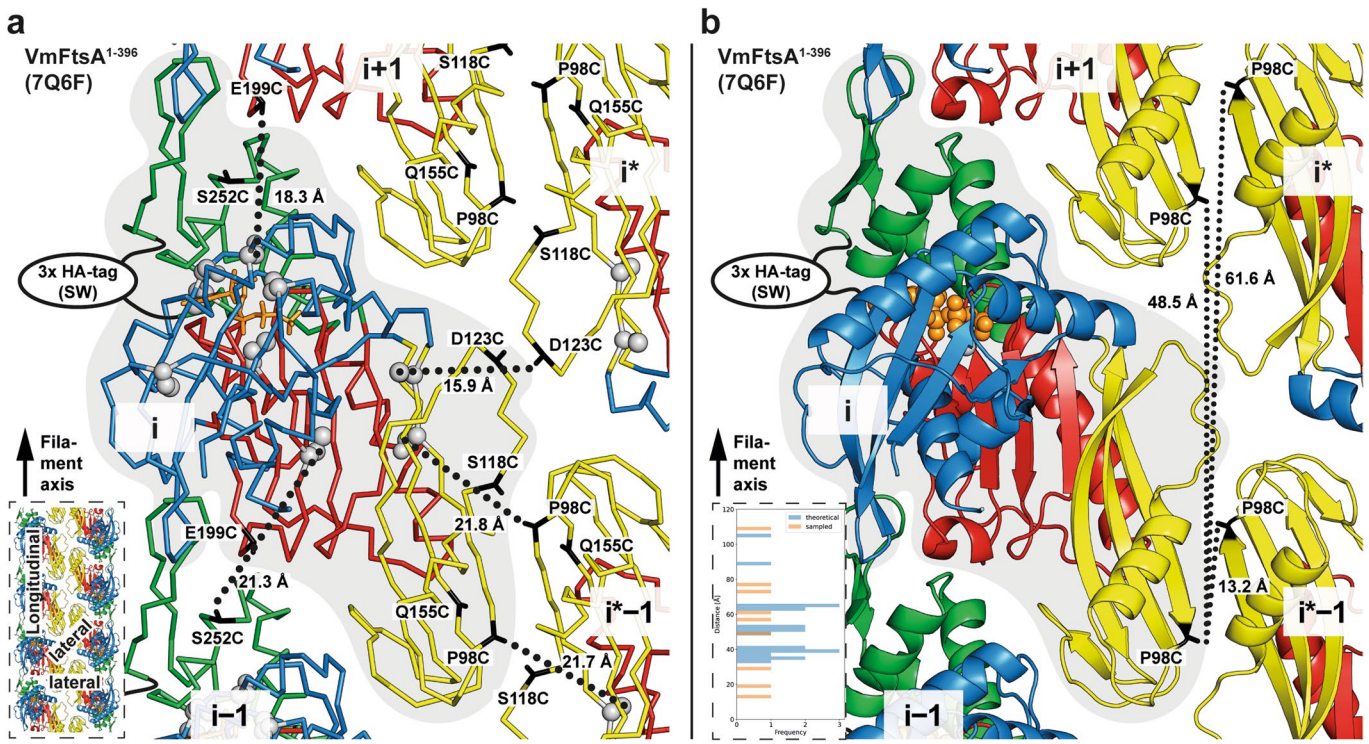

Extended Data Fig. 5 | Distances between endogenous and mutated cysteines in the FtsA double filament. a, Positions of endogenous cysteines in EcFtsA (grey spheres) and of all cysteine mutations used for *in vivo* cysteine cross-linking (black sticks) (Fig. 5a) are highlighted on the VmFtsA double filament structure (PDB 7Q6F). Dotted lines indicate intermolecular C_β-C_β (putative cross-link) distances between selected cysteine mutations and the closest endogenous cysteine, the shortest distance being 15.9 Å ($FtsA_i$ C163-$FtsA_{i^*}$ D123C). The inset highlights the interfaces in the VmFtsA double filament. SW: sandwich fusion. **b**, Single cysteine point mutations serve as controls for distance-independent intermolecular cross-linking because of the symmetry of the FtsA double filament, as illustrated on the example of P98C. The P98C mutation used for *in vivo* cysteine cross-linking is highlighted on the VmFtsA double filament structure (PDB 7Q6F). C_β-C_β distances between intermolecular P98C mutations are indicated by dotted lines. The inset provides a comparison between experimentally sampled intermolecular C_β-C_β distances by single cysteine point mutations (orange) and all intermolecular C_β-C_β distances between amino acids P98, S118, E199 and S252 (blue). Single cysteine point mutations sample intermolecular distances similar to those between double cysteine mutations. Calculated intermolecular C_β-C_β distances were rounded to one digit and duplicate values removed prior to plotting.

nature portfolio

Corresponding author(s): Jan Löwe

Last updated by author(s): Jun 29, 2022

Reporting Summary

Nature Portfolio wishes to improve the reproducibility of the work that we publish. This form provides structure for consistency and transparency in reporting. For further information on Nature Portfolio policies, see our Editorial Policies and the Editorial Policy Checklist.

Statistics

For all statistical analyses, confirm that the following items are present in the figure legend, table legend, main text, or Methods section.

n/a	Confirmed	
☐	☒	The exact sample size (*n*) for each experimental group/condition, given as a discrete number and unit of measurement
☐	☒	A statement on whether measurements were taken from distinct samples or whether the same sample was measured repeatedly
☒	☐	The statistical test(s) used AND whether they are one- or two-sided *Only common tests should be described solely by name; describe more complex techniques in the Methods section.*
☒	☐	A description of all covariates tested
☒	☐	A description of any assumptions or corrections, such as tests of normality and adjustment for multiple comparisons
☐	☒	A full description of the statistical parameters including central tendency (e.g. means) or other basic estimates (e.g. regression coefficient) AND variation (e.g. standard deviation) or associated estimates of uncertainty (e.g. confidence intervals)
☒	☐	For null hypothesis testing, the test statistic (e.g. *F*, *t*, *r*) with confidence intervals, effect sizes, degrees of freedom and *P* value noted *Give P values as exact values whenever suitable.*
☒	☐	For Bayesian analysis, information on the choice of priors and Markov chain Monte Carlo settings
☒	☐	For hierarchical and complex designs, identification of the appropriate level for tests and full reporting of outcomes
☒	☐	Estimates of effect sizes (e.g. Cohen's *d*, Pearson's *r*), indicating how they were calculated

Our web collection on statistics for biologists contains articles on many of the points above.

Software and code

Policy information about availability of computer code

Data collection	Cryo-EM: EPU 1.5 and 2.13, SerialEM 3.9 X-ray crystallography: Diamond Generic Data Acquisition (GDA) software on beamlines i03 and i04
Data analysis	Cryo-EM: MotionCor2, CTFFIND4 and 4.1, RELION-3.0, -3.1 and -4.0 X-ray crystallography: CCP4 suite 7.1, Phaser 2.82 and 2.83, MAIN 2017, Coot 0.8.9.3, REFMAC 5.8, Phenix 1.17.1 Plots: Prism 8.0, Anaconda navigator 1.10.0 running Jupyter Notebook 6.1.4 and Python 3 NMR: MddNMR package 3.2, MARS 1.2, Topspin 3.6.0, NMRFAM-Sparky 1.47 HDX-MS: Protein Lynx Global Server 3.0.3, DynamX 3.0 FDS-AUC: SEDFIT 16, SEDPHAT 15.2, GUSSI 1.4.2 Co-pelleting assay: ImageJ 2.1.0 NGS: breseq v0.35.1

For manuscripts utilizing custom algorithms or software that are central to the research but not yet described in published literature, software must be made available to editors and reviewers. We strongly encourage code deposition in a community repository (e.g. GitHub). See the Nature Portfolio guidelines for submitting code & software for further information.

Data

Policy information about availability of data

All manuscripts must include a data availability statement. This statement should provide the following information, where applicable:

- Accession codes, unique identifiers, or web links for publicly available datasets
- A description of any restrictions on data availability
- For clinical datasets or third party data, please ensure that the statement adheres to our policy

Atomic coordinates have been deposited in the PDB with accession codes 7Q6D (Escherichia coli FtsA1-405), 7Q6G (Xenorhabdus poinarii FtsA1-396), 7Q6F (Vibrio maritimus FtsA1-396, antiparallel double filament) and 7Q6I (Vibrio maritimus FtsA1-396 and FtsN1-29, bent tetramers in antiparallel double filament arrangement). NGS data associated with this study are available from the Sequence Read Archive at BioProject PRJNA852398. PDB entries 1E4F, 1E4G, 2YCH, 3WQT, 3WQU, 3WT0, 4A2A, 4A2B, 4CZJ were used for structural superpositions and analyses.

Coordinate and structure factor files of our interpretations of the VmFtsN1-29 density (Extended Data Figure 3e), annotated vector maps, annotated genomic loci of E. coli strains and a summary of NGS findings for whole genome sequenced strains are available with the paper online. Other data is available upon request.

Field-specific reporting

Please select the one below that is the best fit for your research. If you are not sure, read the appropriate sections before making your selection.

☒ Life sciences ☐ Behavioural & social sciences ☐ Ecological, evolutionary & environmental sciences

For a reference copy of the document with all sections, see nature.com/documents/nr-reporting-summary-flat.pdf

Life sciences study design

All studies must disclose on these points even when the disclosure is negative.

Sample size	Sample sizes were not predetermined and all available data were processed. For EM, at least two grids for each condition were assessed, with at least 3 grid squares being examined resulting in 10-15 images per grid. For the 2D class average in Figure 2e, 1520 micrographs were collected on one grid. For 2D class averages in Figure 4e, 34 micrographs were collected on one grid. Representative images for publication were chosen by eye.
Data exclusions	Cryo-EM: particle sorting and exclusion in RELION followed standard procedures and the remaining particle numbers are mentioned in the methods section
Replication	X-ray crystallography, cryo-EM data collection and RELION processing, NMR, FDS-AUC, NGS: no replicates - X-ray crystallography: multiple crystals were obtained for each condition with variable diffraction strength, only highest resolution datasets were used to solve the respective structures - cryo-EM data collection and RELION processing: at least two independent grids were examined per condition, showing comparable higher order assemblies and arrangements, data were collected on one grid, replication was not attempted as thousands of individual particles are averaged each time - NMR: bulk measurement in solution, therefore not replicated - FDS-AUC: bulk measurement in solution, therefore not replicated, data are in agreement with FP and Co-pelleting experiments - NGS: bulk measurement of the DNA of cells grown in solution, therefore not replicated SPR: achieved at least technical duplicates, EcFtsA1-405 - EcFtsN1-32 was replicated at least 3 times starting from EcFtsA1-405 attachment to the CM5 chip FP: achieved quintuplicates (freshly mixed sample on different days) Co-pelleting: achieved technical duplicates EM: achieved at least duplicates/two grids each (prepared on different days from freshly mixed sample) with at least 3 grid squares examined, EcFtsA-FtsN1-32 double filament formation was observed at least 5 times in negative stain and with two different purifications/batches of EcFtsA and EcFtsN1-32, respectively HDX-MS: achieved technical triplicates that were prepared and analysed in parallel In vivo cysteine crosslinking: achieved biological triplicates (Figure 5c) or duplicates (Figure 5e) (independently grown cultures from one glycerol stock) Growth on solid media: achieved biological triplicate (independently grown plates from glycerol stocks) Growth in liquid media: achieved technical octuplicate (grown in parallel) DIC imaging of exponential phase cultures: achieved biological triplicate (independently grown cultures from glycerol stocks), two of which were imaged using phase contrast and one of which was imaged using DIC
Randomization	No randomisation was performed. N/A for in vitro reconstitutions with purified proteins.
Blinding	No blinding was performed. N/A as no manual sample categorisation was performed, i.e. sample identity was only determined by components in the reaction mixture.

Reporting for specific materials, systems and methods

We require information from authors about some types of materials, experimental systems and methods used in many studies. Here, indicate whether each material, system or method listed is relevant to your study. If you are not sure if a list item applies to your research, read the appropriate section before selecting a response.

Materials & experimental systems

n/a	Involved in the study
☐	☒ Antibodies
☒	☐ Eukaryotic cell lines
☒	☐ Palaeontology and archaeology
☒	☐ Animals and other organisms
☒	☐ Human research participants
☒	☐ Clinical data
☒	☐ Dual use research of concern

Methods

n/a	Involved in the study
☒	☐ ChIP-seq
☒	☐ Flow cytometry
☒	☐ MRI-based neuroimaging

Antibodies

Antibodies used: anti-HA-Peroxidase (Roche 12013819001)

Validation: Antibodies were validated by comparing samples from tagged (presence of signal at expected molecular weight) and untagged strains (absence of signal) in Western Blotting. Additionally, Western Blotting was also performed against a purified HA-tagged protein.